Title
MEASUREMENTS OF THE LINEAR ACCELERATOR EXIT BEAM OP THE BEVATRON INJECTOR

Authors
Allison, Robert W.
Evans, Don M.
Richter, Robert M.
et al.

Publication Date
1966-09-19

UCRL-17001

University of California

Ernest O. Lawrence Radiation Laboratory

MEASUREMENTS OF THE LINEAR-ACCELERATOR EXIST BEAM OF THE BEVATRON INJECTOR

Berkeley, California

DISCLAIMER

Submitted for presentation at the
1966 Linear Accelerator Conference,
Los Alamos, New Mexico, Oct. 3-7,
1966

UCRL-17001
Preprint

UNIVERSITY OF CALIFORNIA
Lawrence Radiation Laboratory
Berkeley, California

AEC Contract No. W-7405-eng-48

MEASUREMENTS OF THE LINEAR-ACCELERATOR EXIT BEAM OF THE BEVATRON INJECTOR

Robert W. Allison, Jr., Don M. Evans, Robert M. Richter,
Allen J. Sherwood, and Emery Zajec

September 19, 1966

MEASUREMENTS OF THE LINEAR-ACCELERATOR EXIT BEAM OF THE BEVATRON INJECTOR*

Robert W. Allison, Jr., Don M. Evans, Robert M. Richter,
Allen J. Sherwood, and Emery Zajec

Lawrence Radiation Laboratory
University of California
Berkeley, California

Abstract

A series of measurements of the characteristics of the linear accelerator (linac) exit beam were made to determine if variations in beam position, emittance, and energy spread were present. These measurements show that beam-position movements due to voltage ripple on the preinjector and linac rf systems occur.

Positions were measured with a resonant 200-MHz induction electrode which detects the center of gravity of the beam. In addition, a series of momentum measurements were made to study filamentation of the linac beam, and the effect of the prebuncher and debuncher. A correlation has been obtained between energy ripple and the beam position jitter. An emittance device that uses a sweeping magnetic field for measuring emittance was constructed, and a preliminary study was made of the linac emittance variation with intensity and tank gradient.

Status of the Bevatron Injector

A brief report on the injector may be of interest. The Bevatron injector (Fig. 1) consists of a 482-keV Cockcroft-Walton preinjector and a 19.3-MeV strong-focusing linear accelerator (linac). The injector was designed to produce 50 mA of high-energy beam but the maximum intensity obtained is 40 mA. To obtain this current, 130 mA of 482-keV ions were required. The beam from the duo-plasmatron source is 60% protons.

The linear accelerator is usually operated at an output intensity of 20 mA. This requires a total input current of 60 mA. The output emittance is 1.8 π cm-mrad;[1] the corresponding input emittance is 9.0 π cm-mrad. The beam pulse is 580 μsec long and the injector operates at 2 pulses per second. The linac synchronous phase is 18 deg, the full width energy spread is $\pm$ 156 keV. The system is reliable, only 3% of the unscheduled down time is caused by the injector. Most of this time is caused by failure of miscellaneous electronic components.

Introduction

In order to understand more fully the process of injection into the Bevatron we have studied the properties of the linear-accelerator exit beam. We have developed two special instruments for these measurements:[2]

(1) A split induction electrode, resonant to the linac frequency, which measures the position of the beam's center of gravity.

(2) A rapid-emittance measuring device that utilizes a sweeping field to measure beam density in the phase plane.

With these measuring tools (and other more conventional instruments) we have studied the linac exit beam to determine if variations in the beam position, emittance, and energy spread were present. These measurements have shown that beam position movements are caused by voltage ripple on the preinjector high voltage and linac rf systems. The instruments are described and the measurement results are given below.

Position Electrodes

Split induction electrodes for beam-position monitoring are used on many accelerators. However, there are difficulties in using such devices on the exit beam of a linear accelerator. Most serious of these problems is that the electrode dimensions are approximately the same as the particle-bunch wavelength; thus careful attention must be given to geometry to avoid phase shifts in the system. Also, if one wishes high accuracy the electrode must be carefully constructed. Finally, in order to obtain signal levels in the mV range (to avoid rf noise problems) the electrodes must also be resonant at the linac tank frequency.

A cylindrically symmetric split induction electrode system has been developed which has a position resolution of $\pm$0.1 mm. The system output is linear with beam displacement (Fig. 2).

Figure 3 shows the coated ceramic electrode used for linac-exit beam-position measurement. The ceramic cylinder is ground on the diameters to a concentricity of $\pm$0.02 mm. The copper electrode material is vacuum-sputtered onto the ceramic to a depth of 0.03 mm. The copper is split so that the projection of each electrode surface in the measurement plane is an isosceles triangle. This longitudinal symmetry eliminates phase shifts due to beam transit-time effects. The pattern is easily produced on a profile tracer lathe, with a small sandblaster for a cutting tool. Two ceramic electrodes, with patterns rotated 90 deg to each other, form a complete position monitor. To assemble a unit one inserts the electrodes into a beam pipe, cylindrical ground planes are inserted into the ends, and the assembly is held in the beam pipe by snap rings. To prevent beam damage, carbon apertures are also inserted in the upstream end. Radiofrequency fingers soldered to the electrodes contact Kovar seals mounted in the beam-tube wall.

These seals have coaxial terminations. Rigid coaxial lines carry the 200-MHz signals to an rf terminating network. To avoid phase shift, we cut the coaxial lines to the same length (within ± 0.08 mm). The lines and network are rigidly mounted to the beam pipe to insure stability.

Of five complete units installed on the linac-exit beam section, three are inserted into steering magnets. Figure 4 is a view of one of these magnet-electrode sets, and shows the electrode rf network. The electrode network is essentially a four-port network, and forms an rf bridge. Figure 5 is a view of the network interior. The electrodes terminate in a folded transmission line. The line is center-tapped and this tap is the electrode sum (Σ) output. An electrostatically shielded loop is located directly under the Σ tap. The loop, which is loosely coupled to the line, is located near a current maximum, and thus reads the line-current unbalance (Δ output). If the network is properly adjusted, this unbalance is proportional to the displacement of the beam center of gravity. The mica capacitors are used to resonate the electrode (the system Q is 200). The line fold is moveable and is used to adjust the line impedance. Two glass trim capacitors are used to balance the resonant line, the Δ loop can also be adjusted. These four adjustments provide enough degrees of freedom to balance the network, since it is symmetric. The network, with the electrode connected, is balanced by driving the Σ output and adjusting the loop position and trim capacitors for minimum Δ output. Then the network is loaded symmetrically with two equal impedances and rebalanced. Iteration between these two conditions makes it possible to insure that the electrode null and beam-tube center coincide. The sum and difference signals are then sent over 125-Ω cables to an analog monitoring rack near the linac block house. The electronics in this rack converts the 200-MHz sum-and-difference signals into position-and-sign information. A block diagram of the electrode electronics is shown in Fig. 6.

In order to obtain useable signals the position electrode cables must be trimmed. With trimming, millivolt signal levels are obtained inside the decoding network. This network (Fig. 7) diode detects the position-difference signal and also forms a discriminator that determines the direction of a beam offset.

The diode-detected Δ signal is amplified in a multi-stage operational amplifier. The feedback loop of this amplifier contains diodes and is nonlinear. The amount of nonlinear gain change is adjustable and is set to just compensate the square-law response of the diode detector. In the operating range the amplifier gain varies from 5 to 500. With an exit beam intensity of 15 mA an output of about 8 V is obtained for a position offset of 1 cm. The linearized displacement signal is then normalized to the exit-beam intensity. This normalizer is a variable-gain "amplifier". The gain of this amplifier is set by the linac exit-section beam intensity (BT3 is used as a reference Fig. 1). Normalizing in this way eliminates Δ signal jitter due to pulse-to-pulse intensity variations. Voltmeter response is plotted in Fig. 2.

Sign information is obtained from the Δ signal in a discriminator that uses the Σ signal as a phase reference. When the beam center passes through the electrode electrical center (null point), the current through the transmission line reverses, changing the polarity of the Δ signal. This 180-deg phase reversal can be detected by discrimination. Referring again to Fig. 7, the Σ signal is connected to the center tap of the discriminator coil. The Δ signal is loosely coupled to the coil by means of a symmetrically placed and electrostatically shielded loop. Thus, at the coil ends, rf signals of $\Sigma + \Delta$ and $\Sigma - \Delta$ are present. These signals are diode-detected and put into a comparator. If the discriminator is balanced, the polarity of the comparator output gives the sign of the beam offset. This signal is put into a negative-and gate and sets a flip-flop whenever the sign is negative and a sample command trigger is present.

The discriminator is balanced by adjusting the coil center-tap location and the trimmer capacitors located at each coil end.

Linac Exit Beam-Center Motion

Using the position electrodes we have observed deflections of the exit beam center. These deflections are caused by changes in the linac quadrupole gradients and linac rf level. Both slow and fast movements occur during the pulse.

1. Slow Deflection

Figures 8 and 9 are plots of the average movements of the beam center with changes in the quadrupole total current and linac tank rf. These data were taken at the center of the injected pulse by reading the voltmeter output and sign at that time (290 μsec after arc-on). The offset was measured on the first two sets of position monitors (P1 and P2) and is plotted as the beam-center displacement and direction at P1. A positive sign represents upward displacement and direction in the vertical plane and displacement and motion towards the Bevatron in the horizontal plane.

The change in beam-center position and direction as a function of total linac quadrupole current is plotted in Figs. 8a and b. The relative strengths of the quadrupoles was unchanged.

At the normal drift-tube magnet settings, the beam center and the nominal geometric axis of the linac do not coincide. The beam is offset by -4.0 mm vertically and +2.1 mm horizontally. The center has a direction of -2.1 mrad vertically and -1.4 mrad horizontally.

A +4% increase in drift-tube magnet current displaces the beam center downwards by 2.2 mm

and increases the downward direction of the center by 2.5 mrad. Horizontally the beam moves toward the Bevatron by 0.7 mm, and the angle is reduced by 0.2 mrad.

Similar movements are observed with changes in the linac tank gradient. (Figs. 9a and b). In general, the optical alignment axis and the ion-optic axis do not coincide, so we expected a small error. However, the vertical displacement is clearly excessive and indicates either a vertical misalignment of the linac or the preinjector. When these data were taken, the injector had just been optically realigned to ±0.1 mm. (This realignment was a movement of the main components, not a resetting of the linac quadrupoles).

Also we were unable to change the vertical offset by adjustment of the linac entrance beam-steering magnets. Steering adjustment caused the output intensity to decrease before any substantial correction of output trajectory occurred. Therefore there probably is a vertical misalignment or aberration in one or more of the linac quadrupoles.

2. Beam Center Motion During the Injector Pulse

During the beam pulse, position movements occur which are randomly superimposed on the slow displacements described above. An early set of measurements made on a prototype electrode (without sign decoding) are shown in Fig. 10. The beam signals read on a beam toroid (BT3) and on the 50-deg spectrometer output cup are also shown. The measurements were made with and without the prebuncher.

The beam-position electrode (P2V) shows a time-dependent oscillation with two frequencies, 2.1 kHz and 50 kHz. The momentum-analyzed beam also shows the same structure, while the spectrometer input beam shows only a small amplitude modulation of 50 kHz. When the prebuncher was removed, most of the lower frequency signal disappeared.

Subsequently an investigation of the fast closed-loop regulator of the preinjector (bouncer) showed that a ±3-kV, 2.1-kHz oscillation was present. The half-amplitude full-width energy acceptance of the linac-prebuncher is 10 keV (without the prebuncher the linac energy acceptance is 50 keV). Evidently the variation in input energy, which represents a large fraction of the energy acceptance, modulates both the linac output energy and the exit beam position. A check of the prebuncher indicated it was operating normally.

We were able to reduce the oscillation to one-eighth of the original amplitude (±400 V regulation) and observed a proportionate decrease in the position and energy sweeping of the beam. The fine ripple structure was found to be due to the linac rf-level regulator, and a similar reduction in the fast sweep of the beam was attained with improvement of this regulator.

We attempted to determine if this sensitivity of position to energy ripple was due to coupling between the linac phase oscillations and the radial motion. The results are shown in Figs. 11 and 12. Slow perturbations were made in the linac rf level and preinjector energy and the beam-position and energy change during the pulse observed.

To measure the energy spread in one pulse, the Bevatron was used as a momentum analyzer. A Faraday cup located in the north tangent tank near the first radial focus was used as an energy detector (with n = 0.67, the radial focus is at 250 deg, the vertical at 205 deg, and the cup at 270 deg). The Bevatron field, which rises at 8.6 kG/sec, was used to sweep the injected beam across the cup face. A 2.5-mm-wide by 92-mm-high slit was placed on the cup.

To prevent interference from multiple turns in the Bevatron, the aperture was closed at the 360-deg point. The cup was inserted into a known good field region, and the injection time adjusted so that the cup intercepted the beam. An ion chamber (Q electrode) which measures circulating charge and is located downstream from the cup, was used to judge when beam interception occurred.

Figure 11a shows the effect of a linac rf-level perturbation on beam position and energy (north Faraday cup). A positive rf perturbation causes the beam to move toward the Bevatron by 0.5 mm and upwards by 2.5 mm. A small notch, at the perturbation time, also appears on the north-Faraday-cup signal. The cup signal is also moved earlier in time, indicating a decrease in energy. A negative perturbation moves the beam away from the Bevatron and down. Both displacements are about 0.5 mm. The north-Faraday-cup signal is again notched and displaced in time. No effect on the time structure of the beam amplitude could be observed from the perturbation.

The north-cup response was also observed with perturbations on the electrostatic inflector and beam chopper (Fig. 1). No change in the cup signal's shape or timing was observed with either a radial or vertical position shift. If the perturbations were large, an amplitude decrease occurred. We therefore concluded that the north Faraday cup was acting as a true spectrometer.

We then studied the effect of a time shift in the linac rf perturbation on the spectrometer response. The results are shown in Fig. 11b. A positive perturbation moves the cup signal earlier in time and notches the signal at the perbation occurrence time. A negative perturbation produces an opposite effect. A slow perturbation (such as the one above) changes the linac synchronous phase, producing a shift in output energy (cup-time variation) and energy spread (change of cup-signal shape). Finally, the prebuncher was disconnected and the north cup signal observed. The cup-signal shape showed the

filamentation of the linac exit-beam energy spread as the tank rf level was changed. Therefore we believe that we were measuring the linear-accelerator energy-time-structure variation during the injector pulse. Thus a correlation exists between the beam center-of-gravity motion and the phase motion of the linear accelerator. Figure 12 shows the results of bouncer perturbations. These results are consistent with that obtained with linac-tank rf perturbations.

It is our opinion that vertical misalignment in the linear accelerator enhances the coupling, which exists for all linear accelerators, between the phase motion and the radial oscillation amplitude.[3] The result of this enhanced coupling is a fast deflection of the linear-accelerator exit beam.

Emittance Measurement Using a Swept Magnet

Most of the techniques used for emittance measurement require data reduction before the phase contour is obtained. The convenience of an instrument that directly displays such contours is obvious. By using a swept field to move a beam across a detector, one can measure and directly display the contour of a beam in the phase plane in 50 injector pulses. (We cannot claim to be the originators of this technique; it was pointed out to us by Vosicki of CERN.[4]) We have constructed such a device and are using it to measure the emittance of the linac exit beam. Figure 13 is a functional diagram of the equipment. Two slits, which are offset, are located at the entrance and exit of the deflecting magnet. The exit slit is mounted on a Faraday cup. The slits are positioned by a slo-syn motor. A voltage proportional to slit position is read from a helipot connected to the slit drive. The offset between the slits can be adjusted by driving the slo-syn with the clutch disengaged (moving only the cup). A flux loop is inserted into the field region, so that it samples the integrated field between the slits. The loop is connected to an integrator, which can be clamped to zero output. The voltage output of the integrator reads the total $\int$Bdl of the magnet. The cup signal is amplified and then used as the input of two voltage discriminators. The discriminator outputs are summed, and the sum output intensity modulates an oscilloscope. The vertical and horizontal inputs of the oscilloscope are connected to the integrator output and slit-position helipot, respectively.

To obtain a phase-plane contour, the slits are located in the beam and their offset adjusted so no signal is observed on the Faraday cup with the magnet off. Then the slits are placed at the beam edge. At the start of the injector pulse, the deflecting magnet is pulsed, and the field rises until at the end of the beam pulse it reaches its maximum integral of 10^4 G-in. The narrow beam, passed by the first slit is therefore swept across the cup face. If the slits are narrow, the image width is proportional to the beam divergence, and the Faraday-cup output is proportional to the phase-plane density of the beam at the first slit position. The change in $\int$Bdl required to just sweep the slit image across the cup is proportional to the angle in the beam. The cup signal is proportional to the phase-space integrated partial-density function (IPDF)[5] $D(xx')$ evaluated at the first slit position, x_i. A constant value of D is obtained by setting the discriminator at a level C_1. Then (see Fig. 13) the discriminator signal appears only when the cup signal exceeds C_1. A vertical line is therefore traced on the oscilloscope (in Fig. 13, the line consists of two segments).

The length of the line is proportional to the total angle enclosed by contour at $x = x_i$. After the beam pulse, the magnetic field decays to zero, the integrator is shorted and the slits are moved to a new location, the integrator is unshorted, and the process is repeated. The result is another line whose length is proportional to the angle contained within the contour at $x = x_{i+1}$. The phase-plane contour is the boundary which just encloses all the lines obtained. This equipment, as shown in Fig. 13, takes two contours simultaneously by modulating the scope-trace intensity.

The instrument, partially assembled, is shown in Fig. 14. In order to obtain 10^4 G-in. in 580 μsec, the magnet is pulsed at 600 V, to a peak current of 250 A. The integrated field is uniform to ±1/4%. The magnet tank is epoxy, painted with silver to eliminate charge build-up. A clear aperture of 7.6 cm is provided for the beam, when the equipment is not in use. Because of the large magnet aperture, fringing fields exist past the slits. But because of eddy currents in the magnet yoke it takes 3 msec for these fields to propagate to the slits. The slits are 4-mm-thick and 0.4-mm-wide carbon. The front slit is mounted on a water-cooled plate. The cup is rf-shielded and has a one-point ground to minimize noise pickup. Currents of 10^{-8} A can be read using the amplifier. The large cylindrical ends serve as bearing surfaces and permit rotation of the entire unit through 90 deg when measuring the emittance of the vertical plane. Rotary vacuum seals are used at each end of the emittance equipment.

Figure 15 shows the equipment installed on the linac exit beam line.

There are two problems in making measurements using this technique:

(1) Beam angles are selected in a time-dependent manner--negative angles first, positive angles last. Therefore, care must be taken if the emittance is time-dependent.

(2) The magnet disperses the beam, and therefore the measured emittance is increased by an amount proportional to the momentum spread of the beam.

The problem of a time-dependent emittance jitter can be partially investigated by making a second measurement of the same beam with the equipment rotated by 180 deg, reversing the

direction of sweep and inverting the selection of angle. The two contours are then superimposed; if there is time jitter in average angle they will not be the same. A symmetric variation of angular spread would not be identifiable.

We cannot avoid the dispersing error, but we feel that an enlarged contour is still quite useful. (In fact, for low-energy work we have been able to display the P^+, H_2^+, and H_3^+ emittances simultaneously).

For the measurements presented below, the equipment resolution for a Gaussian beam distribution was ±0.1 π cm-mrad.

Linac Exit-Beam Emittance

Using the equipment described above, we made a preliminary study of the linac exit beam emittance. Figures 16 and 17 show the oscilloscope presentation of the horizontal and vertical emittance. The beam intensity was 18 mA, the outer-contour IPDF level 0.9, and the inner-contour level 0.5. The horizontal emittance was 2.2 π cm-mrad, the vertical 2.1 π cm-mrad (IPDF ϵ = 0.9). The corresponding 0.5-level contour emittances were 0.5 π cm-mrad and 0.45 π cm-mrad. Figure 18 shows the beam pulse, magnet $\int$Bdl, and the Faraday-cup amplifier output as a function of time, for one slit position.

At a constant output of 18 mA a series of contour-level emittance measurements were taken. Figures 19, 20, and 21 shows the results. The emittance enclosed by a given IPDF level curve is plotted as a function of level ϵ in Fig. 19 for both transverse planes. The emittance of the IPDF as a function of ϵ is not linear. Both planes have essentially the same emittance, at a given ϵ. Figures 20 and 21 are plots of the maximum radius and angle contained within a given IPDF level. The distribution of maximum angle and radius in the two planes is not the same (a consequence of most systems with strong focusing).

We also measured the horizontal emittance as a function of output beam current and linac rf tank level (synchronous phase). The results are plotted in Figs. 22 and 23. The IPDF contour level is 0.9. There is a definite increase in emittance with current which is proportional to the known emittance growth of the preinjector beam with current. No significant variation in emittance was observed with linac tank level change.

Linac Energy Spectra

A great deal of interest has been shown in computing the expected energy spectra of a linear accelerator and correlating the theoretical values with the observed spectra.[6] We have measured the linac exit-beam energy spread (using the 50-deg spectrometer) for three end-tuner settings as a function of linac tank rf level and preinjector energy. These data are presented in Figs. 24, 25, and 26. The mean energy is plotted as a function of tank level for each end-tuner setting in Fig. 27. (The graph scale is expanded at the high-energy end). The preinjector energy was 482 keV (normal setting). The prebuncher was removed. The spectrometer resolution was ±28 keV, the absolute calibration error ($\int$Bdl) ±5%. The sensitivity of the spectra to tank tilt has prevented us from doing a detailed comparison with theory. Although the spectra and output energy differences between the end-tuner runs are obvious, we were unable to see a significant change in the linac rf field on the tank wall probes. An evaluation of the original linac flattening data convinced us that we only knew the field to within ±5%, and that no known correlation existed between the axial-field measurements and the wall probes. Without a detailed knowledge of the field law in the tank, no detailed theoretical comparisons can be made.

However, we decided to see how different the linac was from a perfect, constant-gradient, linear accelerator. From Fig. 27 one can obtain the synchronous phase of the machine since

$$\cos\phi_s = \frac{V_{th}}{V_{0p}}, \qquad (1)$$

where V_{0p} is the rf level at which the tank is running and V_{th} is the rf level where a beam of the proper energy is first observed. Figure 28 shows a plot of the synchronous phase vs rf level for constant input energy (482 keV) for three end-tuner settings.

We then computed the number of phase oscillations in the linear accelerator in the following way. The tank was assumed flat, the output kinetic energy and input energy were measured, and the average gradient E_0 of the linac computed from

$$T - T_0 = \int eE_0T(0)\cos\phi_s\, d_z \approx eE_0\overline{T(0)}\cos\phi_s Z\Big]_0^L \qquad (2)$$

where L is the length of the linac tank, T is the total output energy, and T_0 is the total input energy. The synchronous phase, ϕ_s, and the average transit-time factor, $\overline{T(0)}$, were considered to be constant. The average transit time was taken to be equal to 0.84, and ϕ_s was determined from the threshold curves and Eq. (1).

Once E_0 is known, the phase change of the machine with E_0 and ϕ_s can be obtained from

$$\phi = \int_0^t \omega_s\, dt = \int_0^L \omega_s \frac{dz}{c\beta_s(z)} \qquad (3)$$

by expressing $\beta(z)$ in terms of E_0. (Here ω_s is the instantaneous angular frequency of the phase oscillation.) Expanding (3), we obtain

$$\phi = \int_0^L \left[\frac{-\pi_e E_0 T(0)^{\sin\phi_s}}{m\lambda c^2}\right] \frac{dz}{\beta_s(z)^{3/2}}. \qquad (4)$$

$\beta_s(z)$ is obtained by assuming that all the gap voltage goes into velocity, so that $m = m_0$. Using Eq. (2), we have

$$\beta_s = \left[\frac{2eE_0 \overline{T(0)} L \cos \phi_s}{m_0 c^2} + \beta_0^2 \right]^{1/2}, \quad (5)$$

where λ is the wavelength of the rf and β_0 the input velocity. Then n, the number of phase oscillations in the linac is equal to

$$n = \left| \frac{2K}{\pi a} \right| \left[(aL + \beta_0^2)^{1/4} - \beta_0^{1/2} \right] \quad (6)$$

where

$$K = \left[\frac{-\pi e E_0 \overline{T(0)} \sin \phi_s}{m_0 c^2 \lambda} \right]^{1/2}$$

and

$$a = \left[\frac{2eE_0 \overline{T(0)} \cos \phi_s}{m_0 c^2} \right].$$

The theoretical curves generated by Eq. (6) are compared with the measured phase oscillations in Fig. 29. (Only the data of Fig. 26 was reduced). In counting phase oscillations from energy spectra, we assumed that at threshold N = 0 and at every half phase oscillation a symmetrical energy spectrum is produced. For several of these points (for example, n = 1 for 482 keV) the rf level was picked by change of symmetry in the spectra. The experimental curve rises more sharply than does the theoretical, but the relative features are the same. The lack of detailed agreement, we feel, can be adequately accounted for by our uncertain knowledge of the rf field, error in the measurement of the input and output energy, and the difficulty of accurately determining the threshold.

The effect of the prebuncher voltage at two tank levels is plotted in Fig. 30. The normal operating voltage is 12 V (buncher diode volts). A transmission gain of two is achieved when the prebuncher is operating.

The effect of the debuncher on the spectra is shown in Fig. 31. It is interesting to note that at a tank level of 930 the full-width energy spread is not affected, while at 960 a reduction of two is achieved. The debuncher is not normally used. Tests are being conducted to determine if the Bevatron betatron-oscillation amplitude can be reduced by raising the linac-exit beam energy during injection, using the debuncher. In this mode we have observed a 400-keV shift of equilibrium energy with 9 V on the debuncher rf monitoring diode.

Conclusion

Measurements of the linac exit beam disclosed a beam-position offset which is probably due to vertically misaligned quadrupoles in the linear accelerator. This offset was composed of a deflecting component due to the quadrupole field, and of a fast sweep in position which was correlated with energy ripple.

If such misalignments with a resultant average offset and coupled sweep in position occur on a long accelerator, beam loss can be experienced. Split induction electrodes are valuable aids in minimizing and controlling such phenomena.

A rapid-emittance device was tested which has an accuracy of ±5%, and the linac exit beam was studied briefly. The two-dimensional phase-density distribution was found to be not uniform. The density distribution, however, was the same for the two planes. The linac-exit horizontal beam emittance was observed to increase with current. (At 18 mA, E_2 was 2Π cm-mrad; at 35 mA, 2.8Π cm-mrad.) This increase is proportional to the preinjector beam-emittance change with current. Therefore no dilution of phase space in the linear accelerator was observed.

We studied filamentation but concluded that we did not know the linac rf field well enough to attempt a detailed correlation of theory and experiment. Application of simple theory gave a rough correlation, although the number of phase oscillations increased more rapidly than predicted by the theoretical curves.

Footnotes and References

*This work was done under the auspices of the U. S. Atomic Energy Commission.

1. Emittances are not normalized to energy. The phase plane area for the emittance above is ΠE = 1.8 Π cm-mrad.
2. Allen J. Sherwood, IEEE Trans. Nucl. Sci. NS-12, 925 (1965).
3. L. Smith and R. L. Gluckstern, Rev. Sci. Instr. 26, 220 (1955).
4. B. Vosicki (private communication) has constructed a unit and used it on the CERN preinjector. T. Sluyters at Brookhaven (private communication) is working on a ferrite two-magnet swept-field device.
5. L. D. Teng, Phase Spaces and Beam Qualities, Argonne National Laboratory report LCT16 March 3, 1960 (unpublished).
6. K. G. Batchelor, Beam Energy Measurements on the Rutherford Laboratory PLA, in Proc. 1964 Conference on Proton Linear Accelerators at MURA (MURA, Madison, Wisconsin, 1964).
7. G. Gallagher-Daggitt, Predicted and Observed Behavior of the ZGS Linac Injector, Argonne National Laboratory report GG-D-3, June 1, 1966, (unpublished).

FIGURE LEGENDS

Fig. 1. Plan view of Bevatron injector showing linac exit section and inflector components (input end not to scale).

Fig. 2. Unnormalized position electrode calibration for 5-, 10-, 15-, and 20-mA beam currents.

Fig. 3. Ceramic position electrode. Note pattern and contact fingers.

Fig. 4. Closeup of steering-magnet position-electrode section (SM3HV-PIHV) with PIH rf network connections. The PIV network is located on the downstream end, opposite side.

Fig. 5. Position electrode rf network.

Fig. 6. Functional diagram of position-electrode electronics.

Fig. 7. Interior view of position-electrode voltmeter showing decoding network.

Fig. 8A. Vertical beam-center position and direction as a function of the % change in the total drift-tube current.

Fig. 8B. Horizontal beam-center position and direction as a function of % change in the total drift-tube current.

Fig. 9A. Vertical beam-center position and direction as a function of linac rf tank level. The operative tank rf level is 930.

Fig. 9B. Horizontal beam-center position and direction as a function of linac rf tank level. The operating tank rf level is 930.

Fig. 10. Effect of prebuncher operation on time-dependent position jitter and amplitude modulation of momentum-analyzed beam.

Fig. 11A. Effect of a slow perturbation of the linac tank rf level on beam position and energy. The dip in the linac envelope at 170 μsec is a sag in rf level due to beam loading. The end of the arc pulse occurs after rf decay, so there is no spike as the beam unloads. This prevents sparkdown of the tank.

Fig. 11B. Response of one-pulse momentum analyzer to linac rf perturbation for two occurence times (linac envelope inverted).

Fig. 12. Effect of a Cockcroft-Walton voltage perturbation on beam position and energy. The beam pulse starts at zero. The perturbations shown are the difference between the normal bouncer-correction voltage (no perturbation) and the change in energy due to the perturbations superimposed on the correction voltage.

Fig. 13. Functional diagram of a swept-field emittance instrument. In the timing diagram, C_1 is the contour. The square waveforms represent the discriminator output. The cross hatches indicate the current contained within each contour.

Fig. 14. View of emittance equipment, showing Faraday cup, magnet, and drive mechanism.

Fig. 15. Linac exit-beam line showing emittance equipment.

Fig. 16. Linac exit-beam horizontal emittance, 18 mA. $\epsilon_1 = 0.9$ [normalized D(xx') level]; $\epsilon_2 = 0.5$.

Fig. 17. Linac exit-beam vertical emittance, 18 mA. $\epsilon_1 = 0.9$; $\epsilon_2 = 0.5$.

Fig. 18. Typical signals from rapid-emittance equipment. (1) Deflecting-magnet integrated field (1V/cm); (2) beam pulse (10 mA/cm); (3) D (xx') (1μA/cm).

Fig. 19. Horizontal and vertical emittance contained within an integrated partial-density function level vs IPDF level. $\phi_s = 18$ deg. Exit current = 18 mA.

Fig. 20. Vertical beam emittance; Maximum radius and angle as a function of the IPDF level. $\phi_s = 18$ deg. Exit current = 18 mA.

Fig. 21. Horizontal beam emittance; Maximum radius and angle as a function of the IPDF level. $\phi_s = 18$ deg. Exit current = 18 mA.

Fig. 22. Linac horizontal emittance ($\epsilon = 0.9$) as a function of linac exit-beam current. $\phi_s = 18$ deg.

Fig. 23. Linac horizontal emittance ($\epsilon = 0.9$) as a function of the linac synchronous phase with the prebuncher operating and disconnected.

Fig. 24. Linac exit-beam energy spread vs tank rf level and preinjector energy. Input-end tuner position is 758.

Fig. 25. Linac exit-beam energy spread vs tank rf level and preinjector energy. Input end tuner position is 768.

Fig. 26. Linac exit-beam energy spread vs tuner rf level and preinjector energy. Input-end tuner position is 778.

Fig. 27. Linac output energy vs tank rf level and input-end tuner position. The preinjector energy is 482 keV.

Fig. 28. Linac synchronous phase vs tank rf level and input-end tuner position.

Fig. 29. Comparison of actual and theoretical phase oscillations as a function of linac tank rf level for these preinjector energies and an input end-tuner position of 778.

Fig. 30. Effect of prebuncher on linac exit-beam energy spread run values: rf level = 930; $\phi_s = 18$ deg. The preinjector energy is 482 keV, for a prebuncher diode reading of 12 V.

Fig. 31. Effect of debuncher on linac exit-beam energy spread as a function of the debuncher voltage for two tank rf levels.

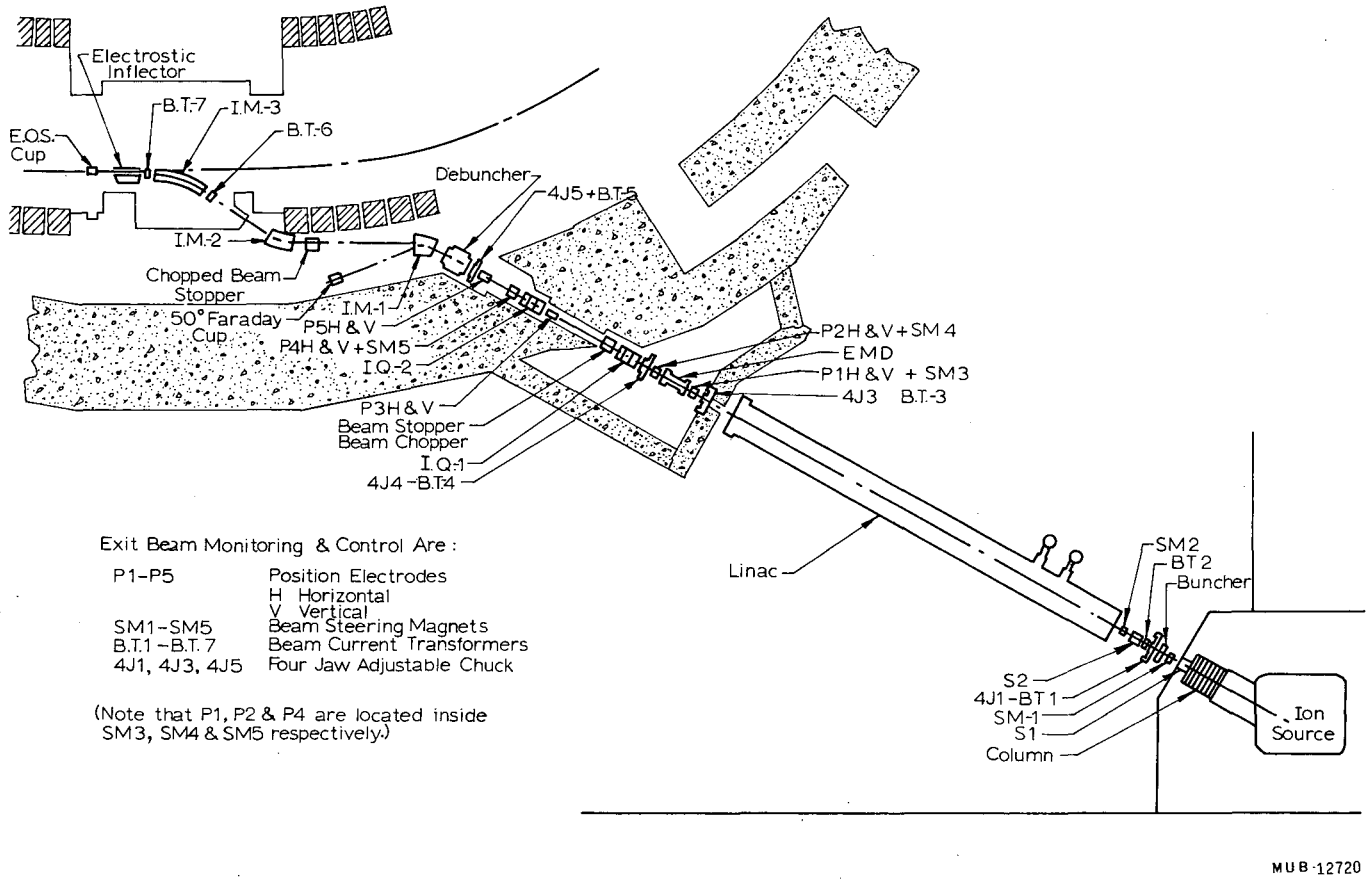
Electrostic Inflector
B.T.-7
I.M.-3
B.T.-6
E.O.S. Cup
Debuncher
4J5+B.T.-5
I.M.-2
Chopped Beam Stopper
I.M.-1
50° Faraday Cup
P5H & V
P4H & V+SM5
I.Q.-2
P3H & V
Beam Stopper
Beam Chopper
I.Q.-1
4J4 -B.T.4
P2H & V+SM 4
EMD
P1H & V + SM3
4J3 B.T.-3
Linac
SM2
BT 2
Buncher
S2
4J1-BT 1
SM-1
S1
Column
Ion Source
Exit Beam Monitoring & Control Are :
P1-P5 Position Electrodes
H Horizontal
V Vertical
SM1-SM5 Beam Steering Magnets
B.T.1-B.T. 7 Beam Current Transformers
4J1, 4J3, 4J5 Four Jaw Adjustable Chuck
(Note that P1, P2 & P4 are located inside SM3, SM4 & SM5 respectively.)
MUB-12720

Fig. 1

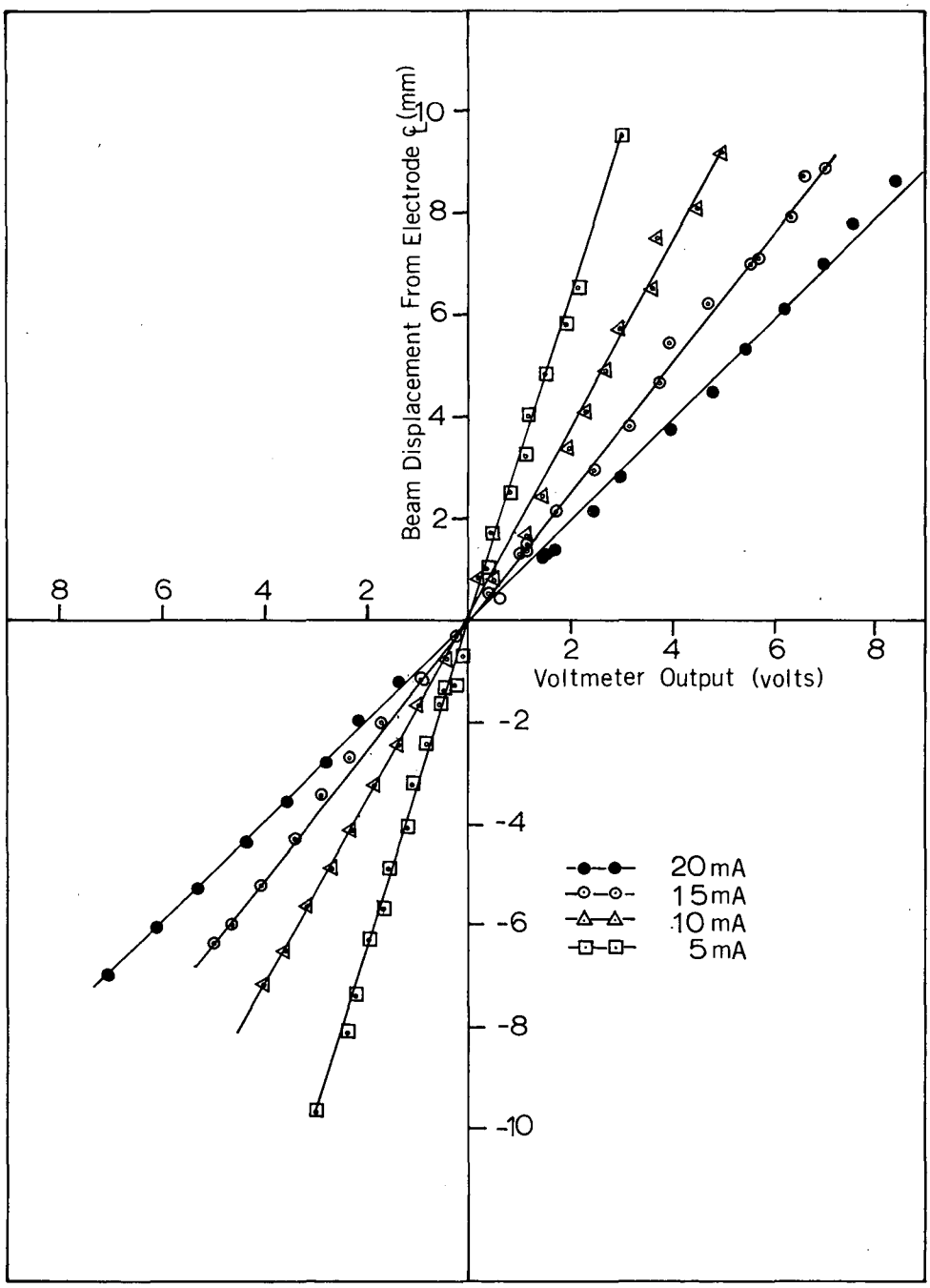

MUB-12892

Fig. 2

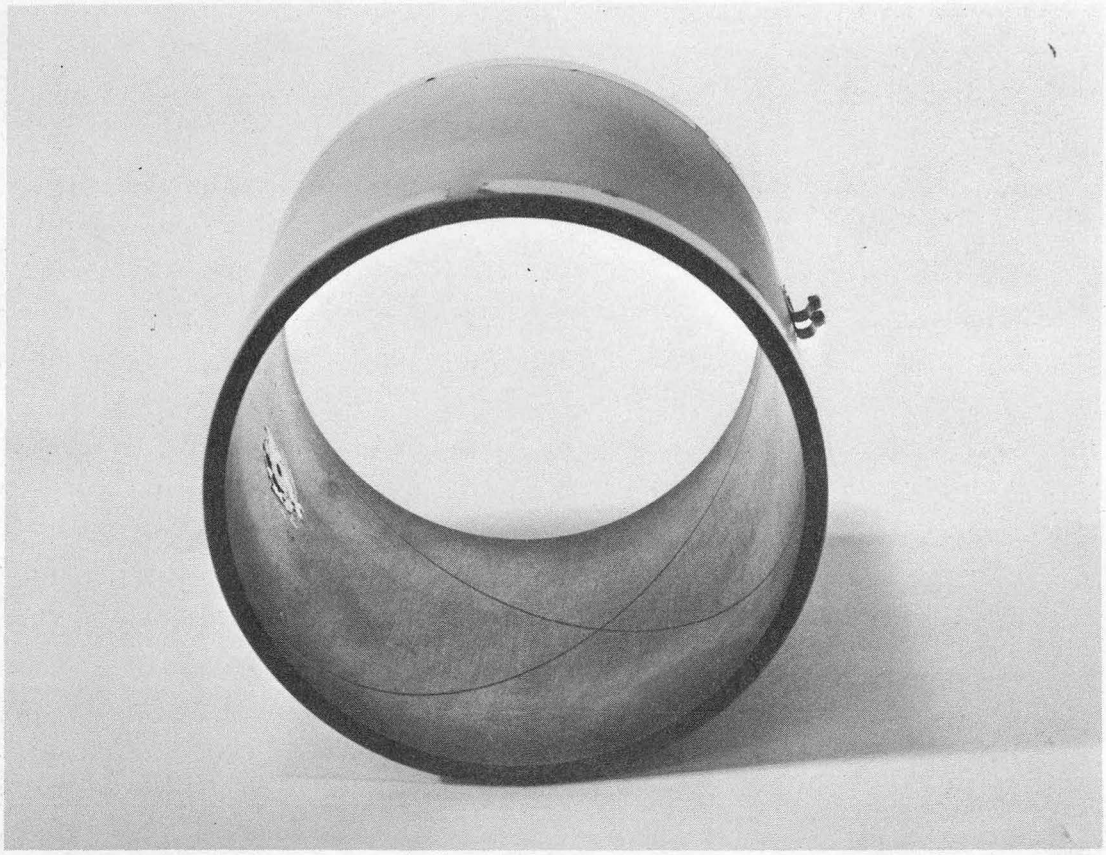

ZN-5915

Fig. 3

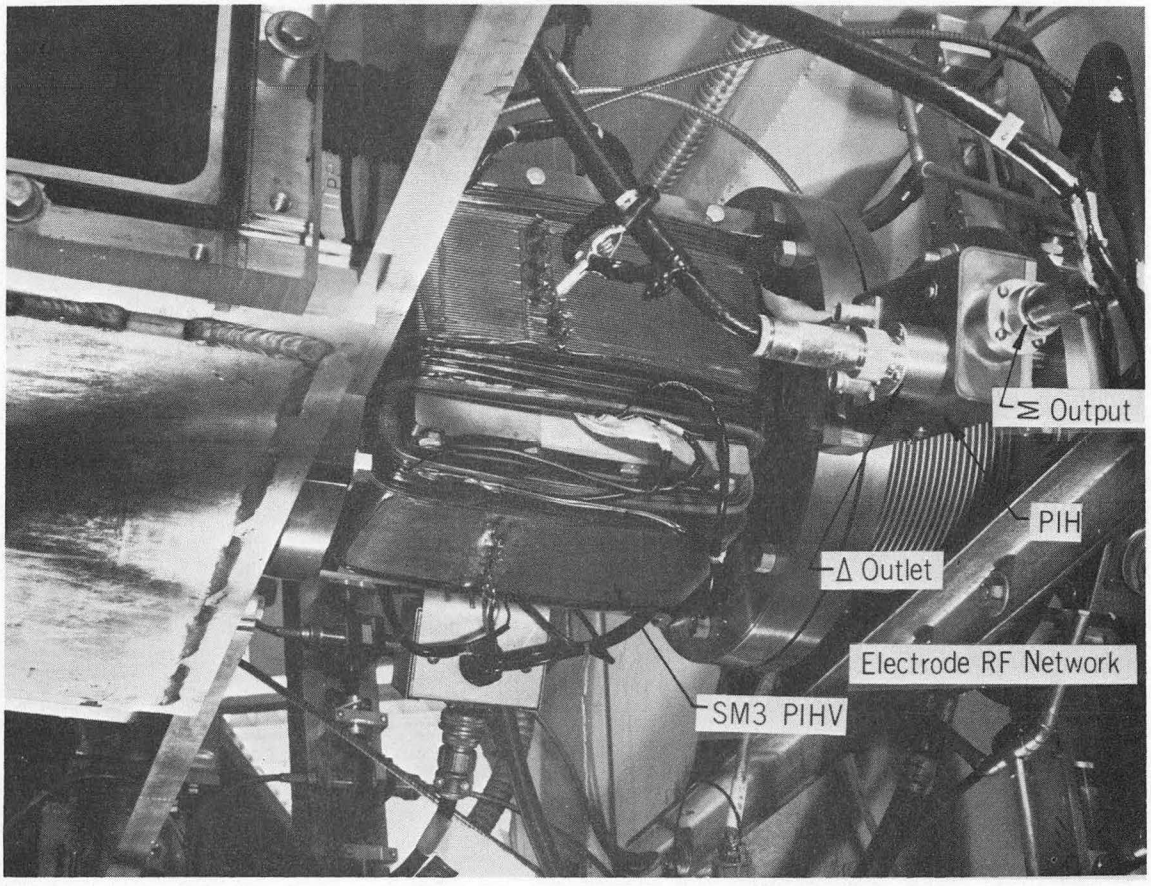

ZN-5916

Fig. 4

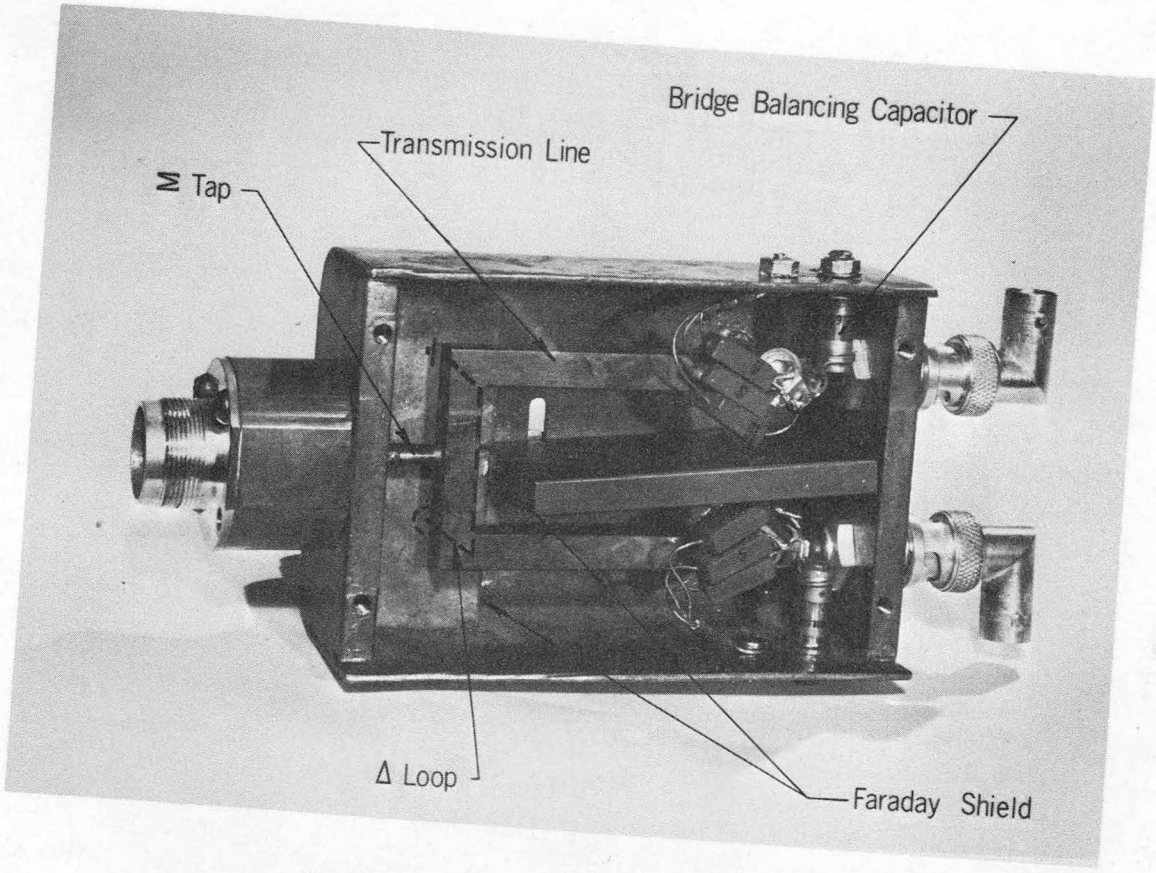
Bridge Balancing Capacitor
Transmission Line
Σ Tap
Δ Loop
Faraday Shield

ZN-5913

Fig. 5

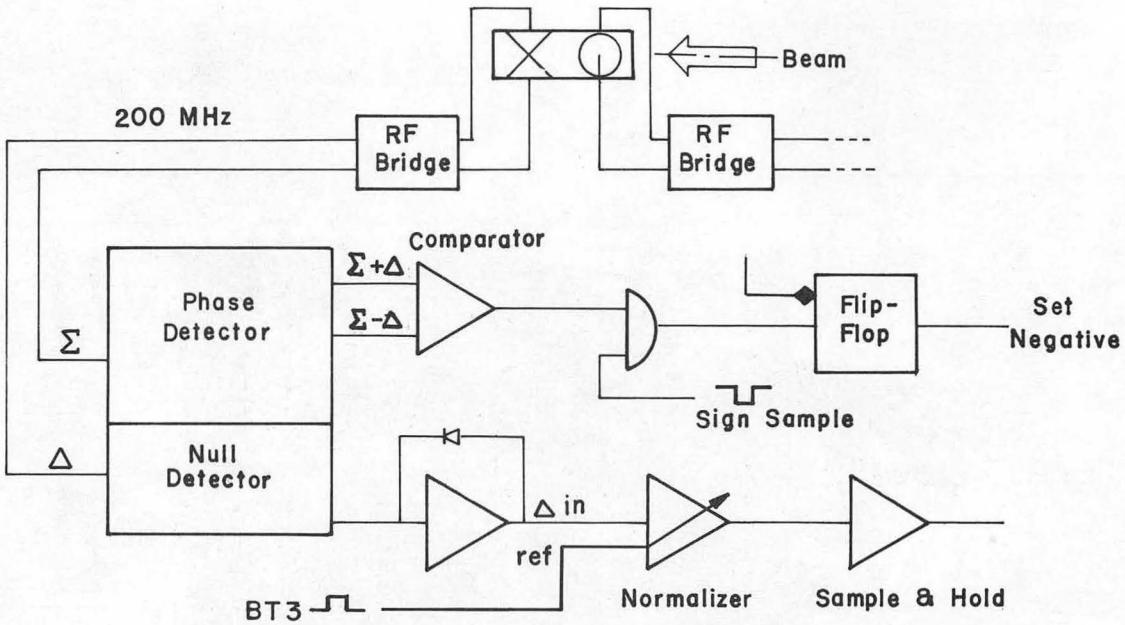

Typical Circuitry for
Position Electrode
P-1 to P-5

MUB-12893

Fig. 6

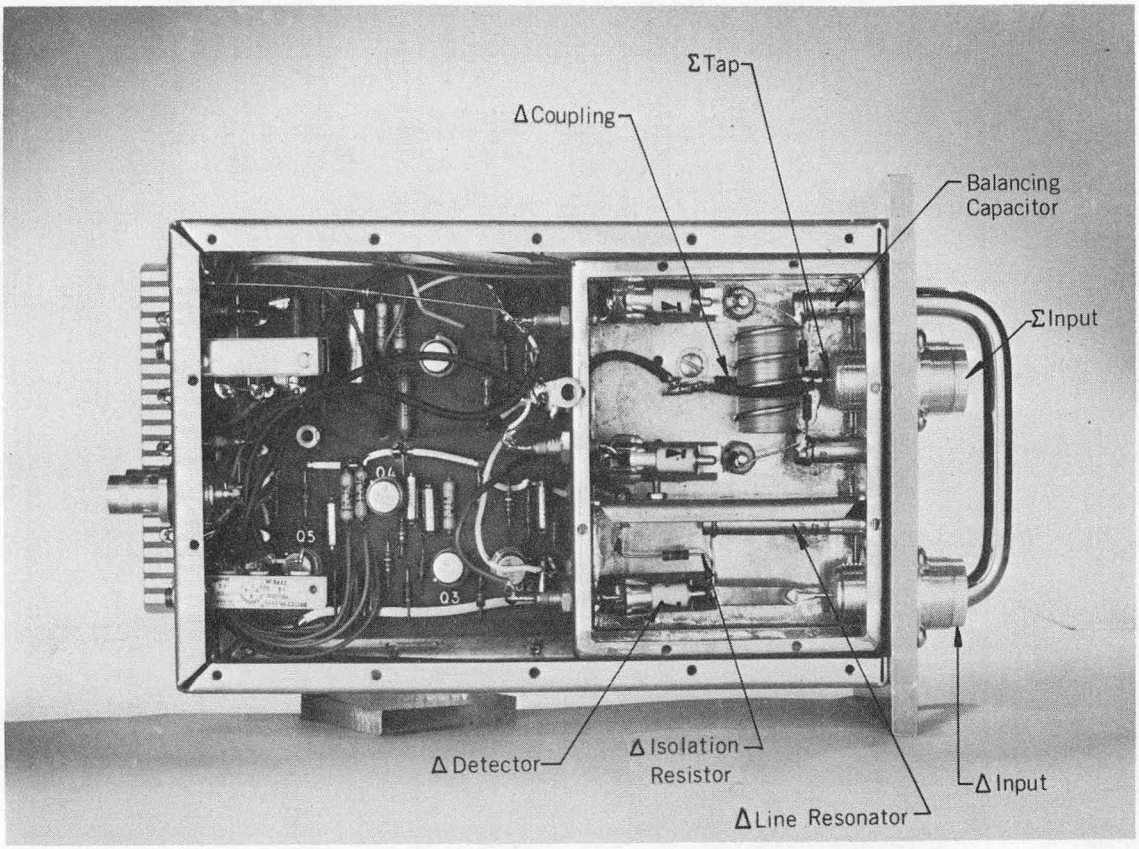
ΣTap
ΔCoupling
Balancing Capacitor
ΣInput
04
05
03
ΔDetector
ΔIsolation Resistor
ΔLine Resonator
ΔInput

ZN-5917

Fig. 7

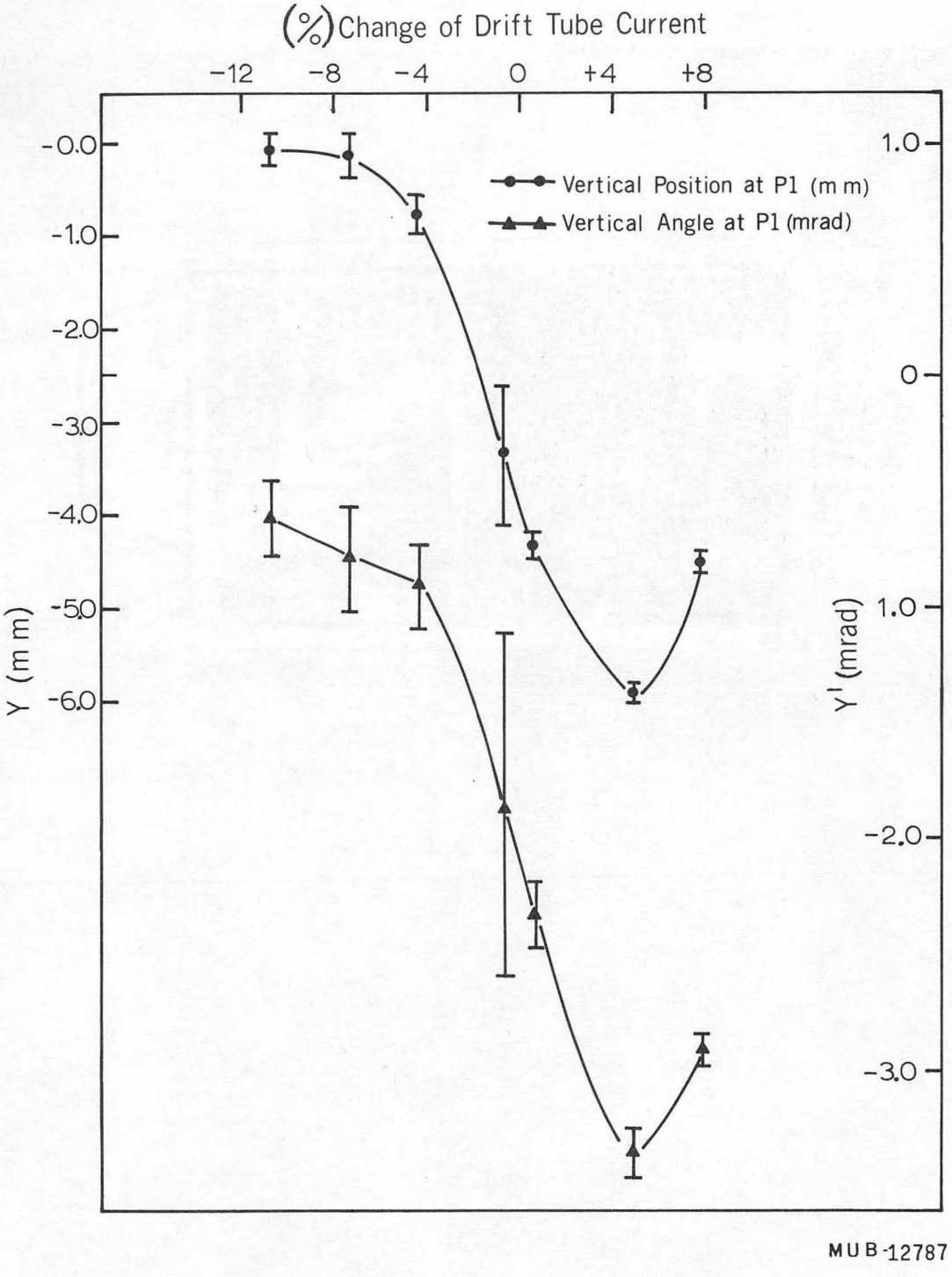
(%) Change of Drift Tube Current
-12
-8
-4
0
+4
+8
-0.0
-1.0
-2.0
-3.0
-4.0
-5.0
-6.0
Y (mm)
1.0
0
1.0
-2.0
-3.0
Y' (mrad)
Vertical Position at P1 (mm)
Vertical Angle at P1 (mrad)
MUB-12787

Fig. 8a

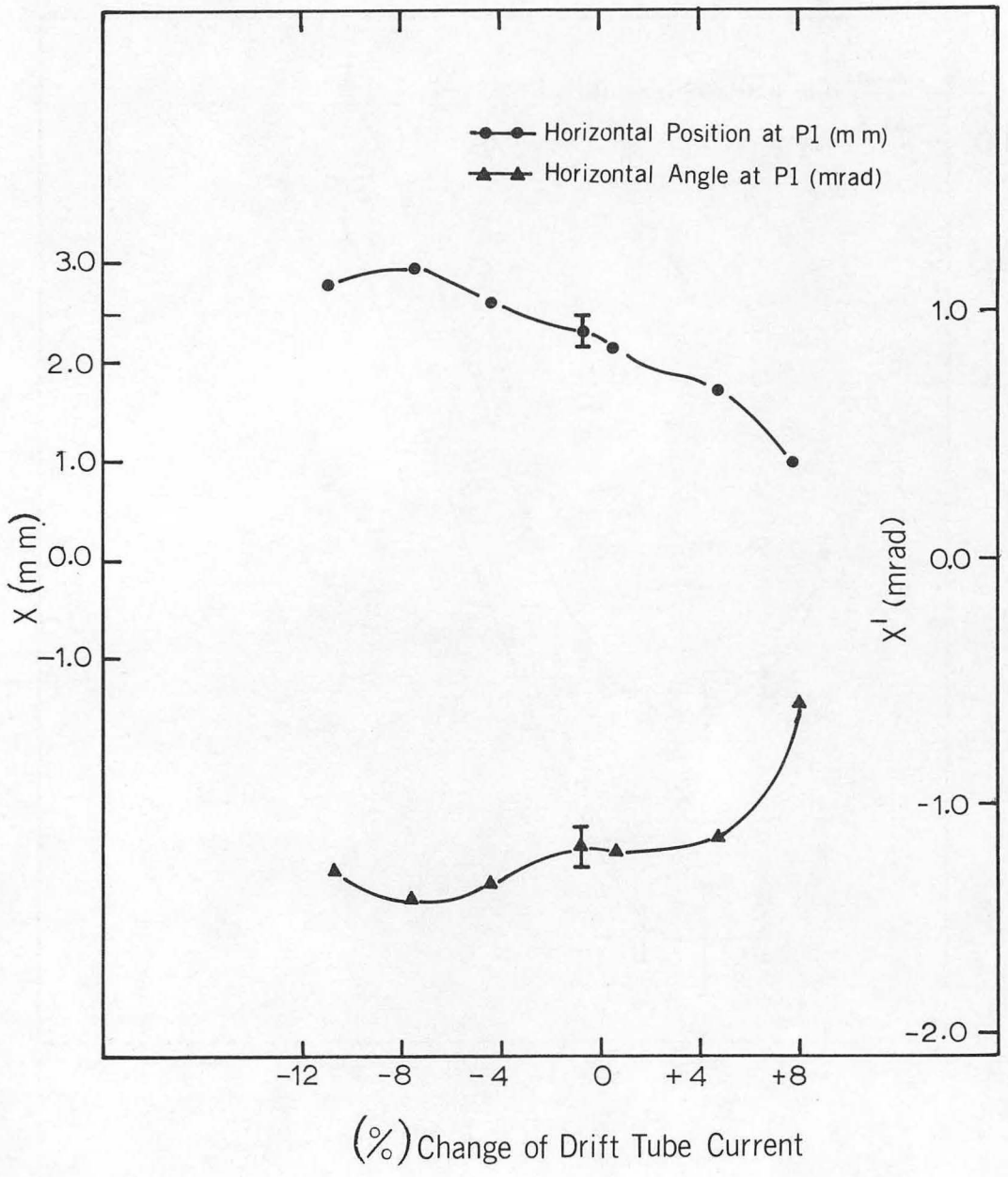
Horizontal Position at P1 (m m)
Horizontal Angle at P1 (mrad)
3.0
2.0
1.0
0.0
-1.0
X (m m)
1.0
0.0
-1.0
-2.0
X' (mrad)
-12
-8
-4
0
+4
+8
(%) Change of Drift Tube Current
MUB-12785

Fig. 8b

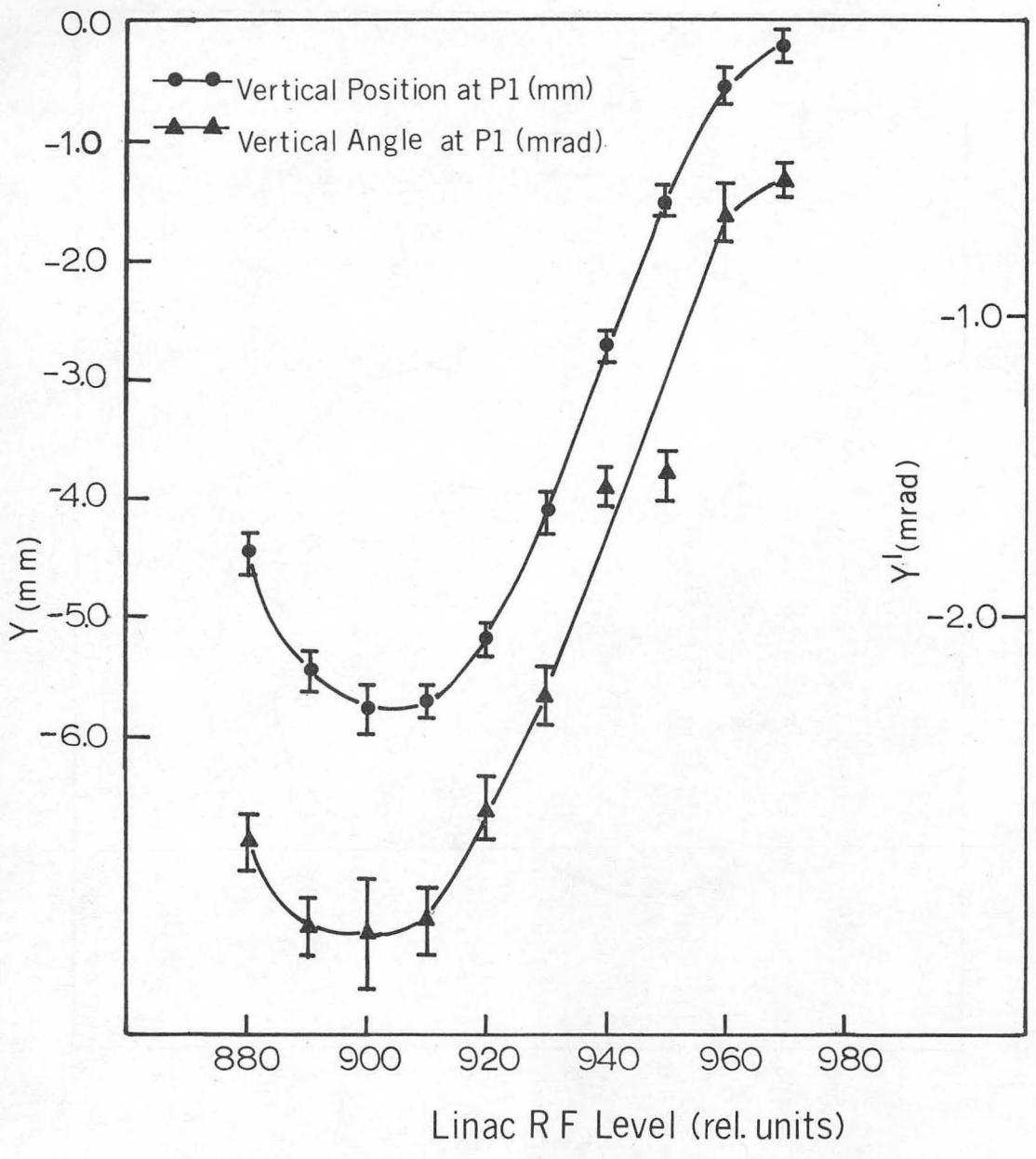
Vertical Position at P1 (mm)
Vertical Angle at P1 (mrad)
0.0
-1.0
-2.0
-3.0
-4.0
-5.0
-6.0
Y (mm)
-1.0
-2.0
Y' (mrad)
880
900
920
940
960
980
Linac R F Level (rel. units)
MUB-12781

Fig. 9a

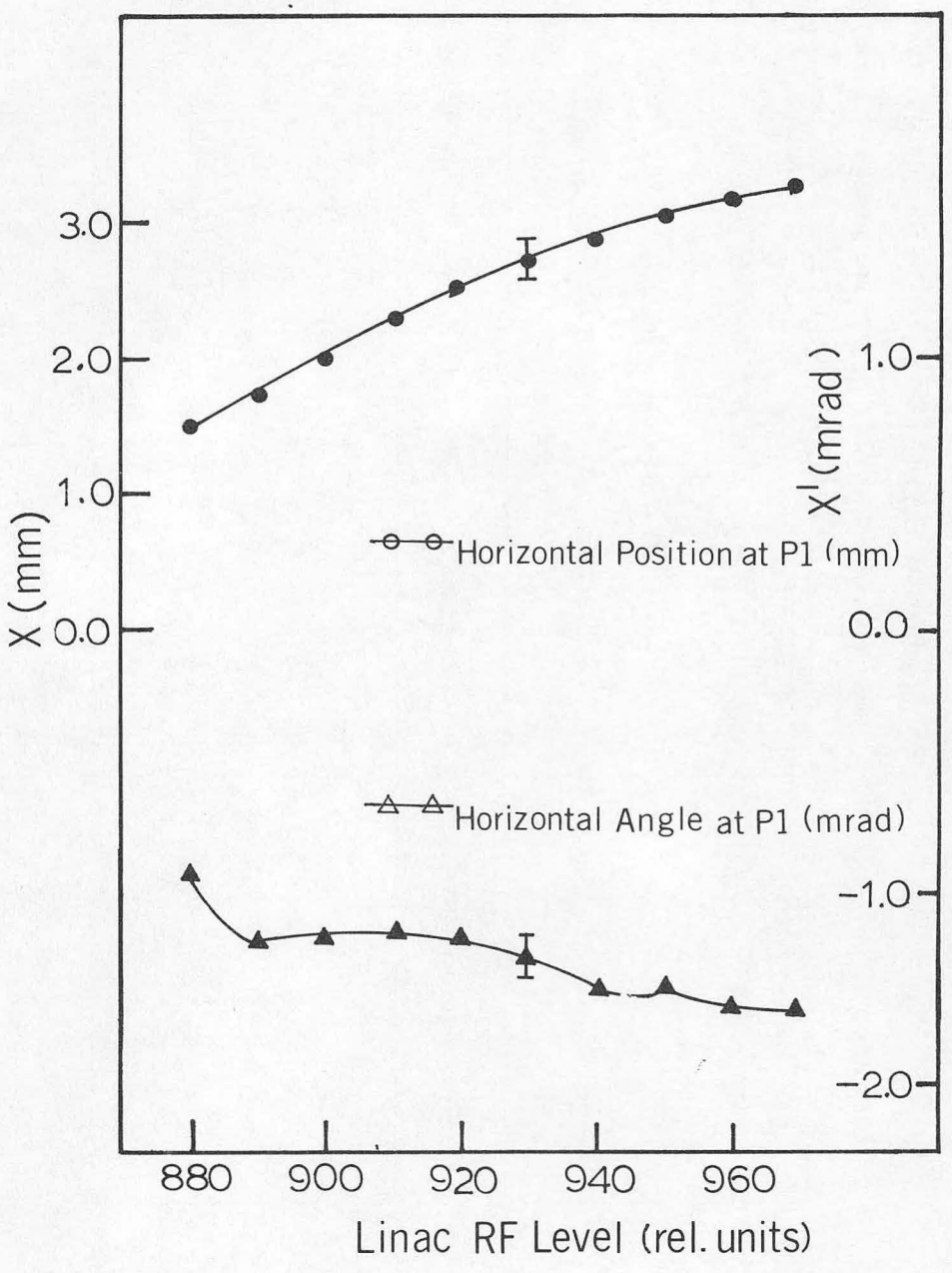
3.0
2.0
1.0
0.0
X (mm)
X' (mrad)
1.0
0.0
-1.0
-2.0
Horizontal Position at P1 (mm)
Horizontal Angle at P1 (mrad)
880
900
920
940
960
Linac RF Level (rel. units)
MUB-12784

Fig. 9b

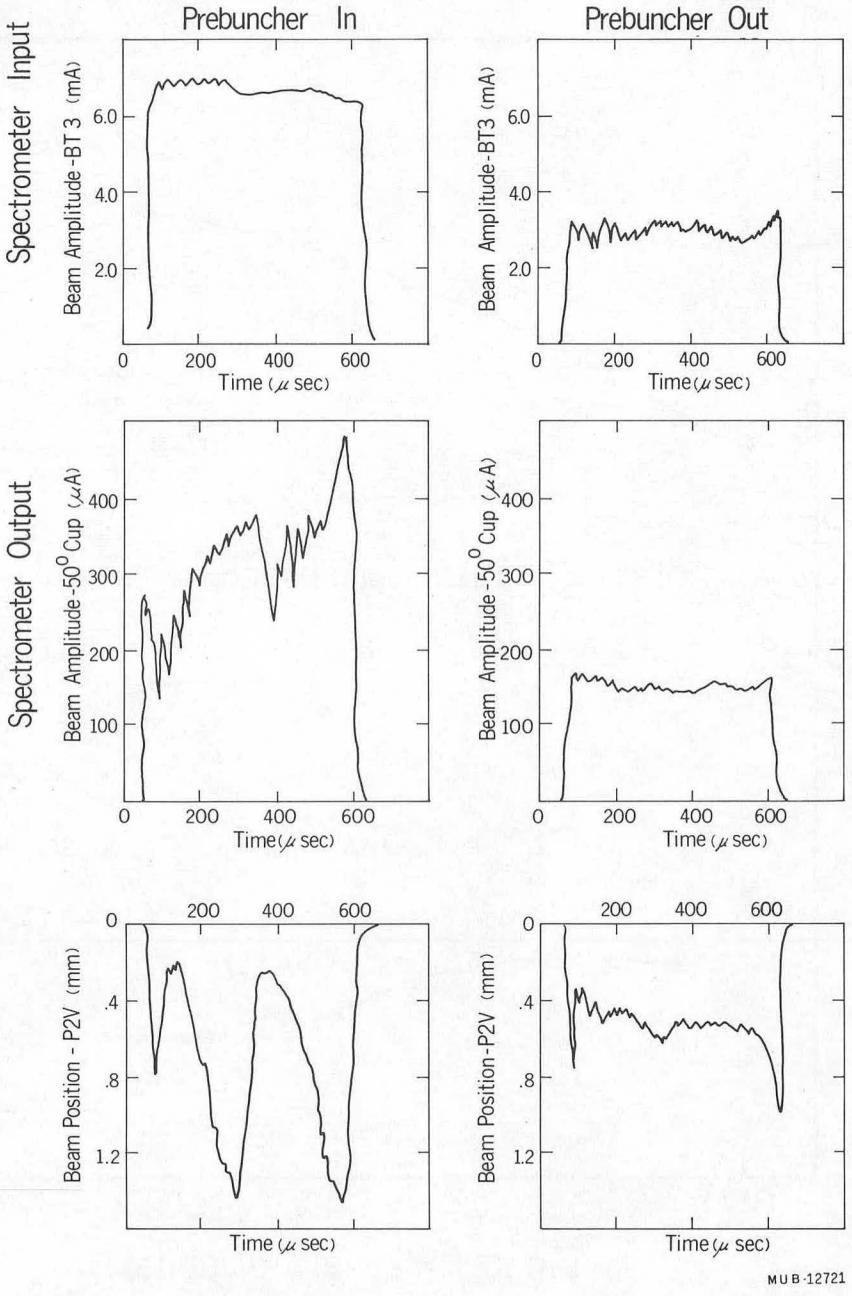
Prebuncher In
Prebuncher Out
Spectrometer Input
Spectrometer Output
Beam Amplitude-BT3 (mA)
Beam Amplitude-50° Cup (μA)
Beam Position - P2V (mm)
Time (μ sec)
0
200
400
600
2.0
4.0
6.0
100
300
.4
.8
1.2
MUB-12721

Fig. 10

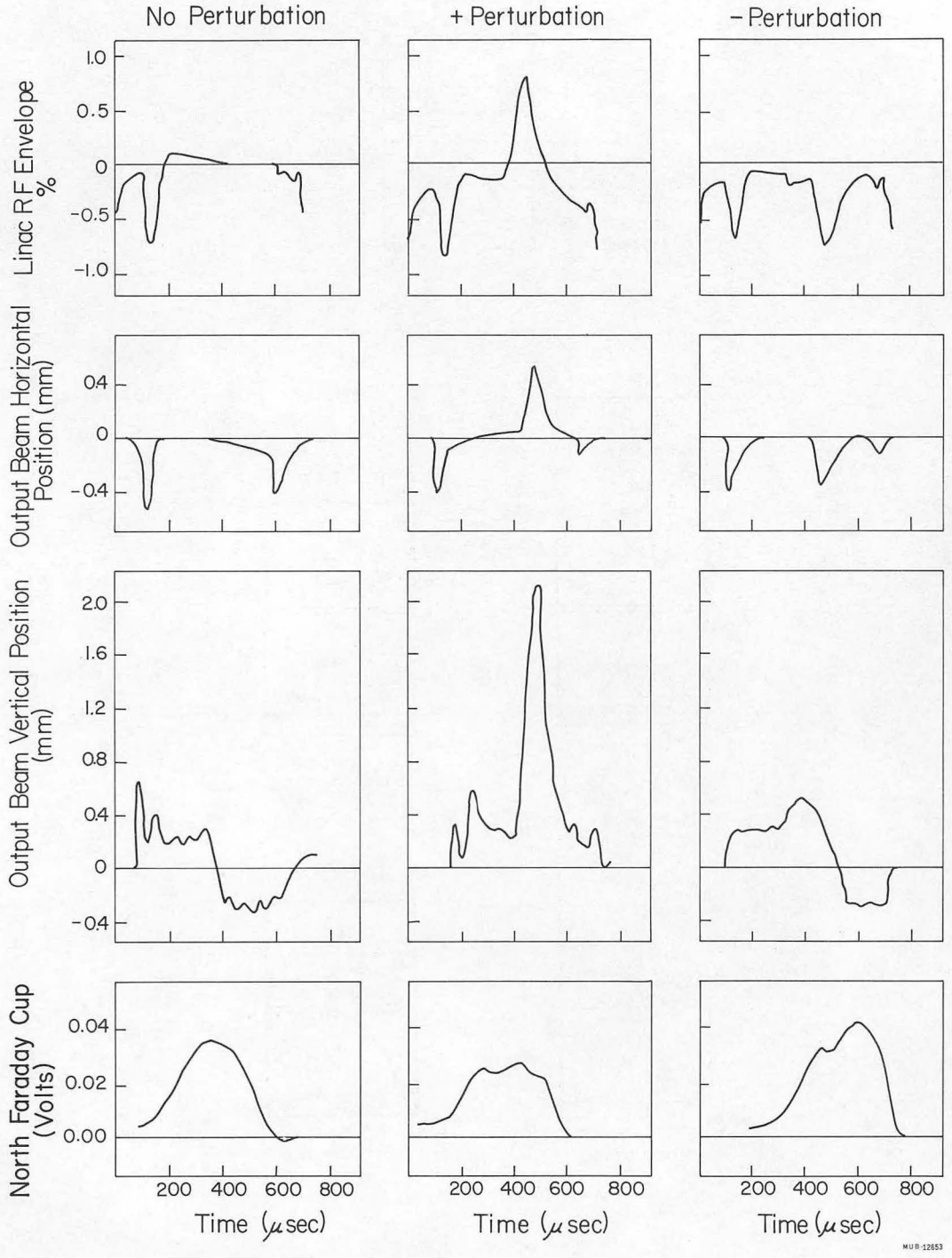
No Perturbation
+ Perturbation
- Perturbation
Linac RF Envelope %
1.0
0.5
0
-0.5
-1.0
Output Beam Horizontal Position (mm)
04
0
-0.4
Output Beam Vertical Position (mm)
2.0
1.6
1.2
0.8
0.4
0
-0.4
North Faraday Cup (Volts)
0.04
0.02
0.00
200 400 600 800
Time (μsec)
MUB-12653

Fig. 11a

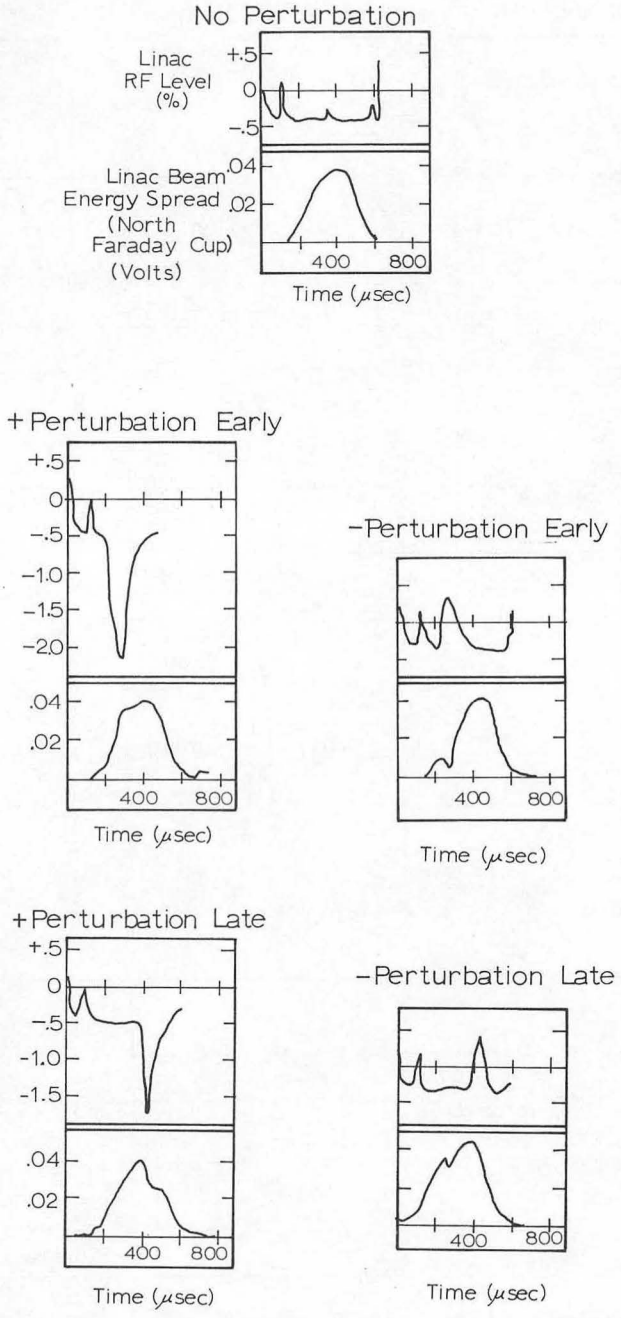
No Perturbation
Linac RF Level (%)
+.5
0
-.5
Linac Beam Energy Spread (North Faraday Cup) (Volts)
.04
.02
400
800
Time (μsec)
+Perturbation Early
+.5
0
-.5
-1.0
-1.5
-2.0
.04
.02
400
800
Time (μsec)
-Perturbation Early
400
800
Time (μsec)
+Perturbation Late
+.5
0
-.5
-1.0
-1.5
.04
.02
400
800
Time (μsec)
-Perturbation Late
400
800
Time (μsec)
MUB-12723

Fig. 11b

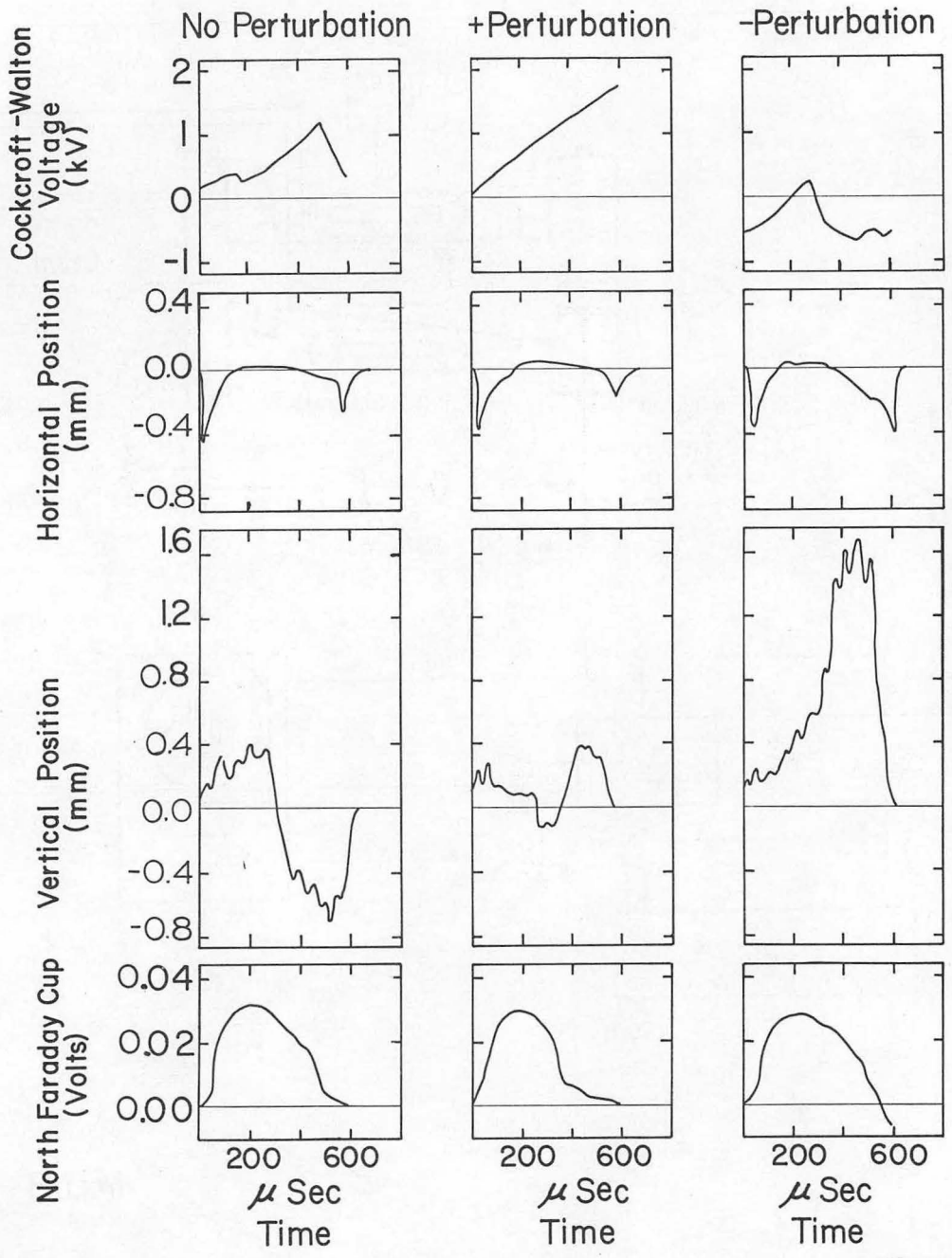
No Perturbation
+Perturbation
-Perturbation
Cockcroft-Walton Voltage (kV)
2
1
0
-1
Horizontal Position (mm)
0.4
0.0
-0.4
-0.8
Vertical Position (mm)
1.6
1.2
0.8
0.4
0.0
-0.4
-0.8
North Faraday Cup (Volts)
0.04
0.02
0.00
200
600
μ Sec
Time
MUB-12788

Fig. 12

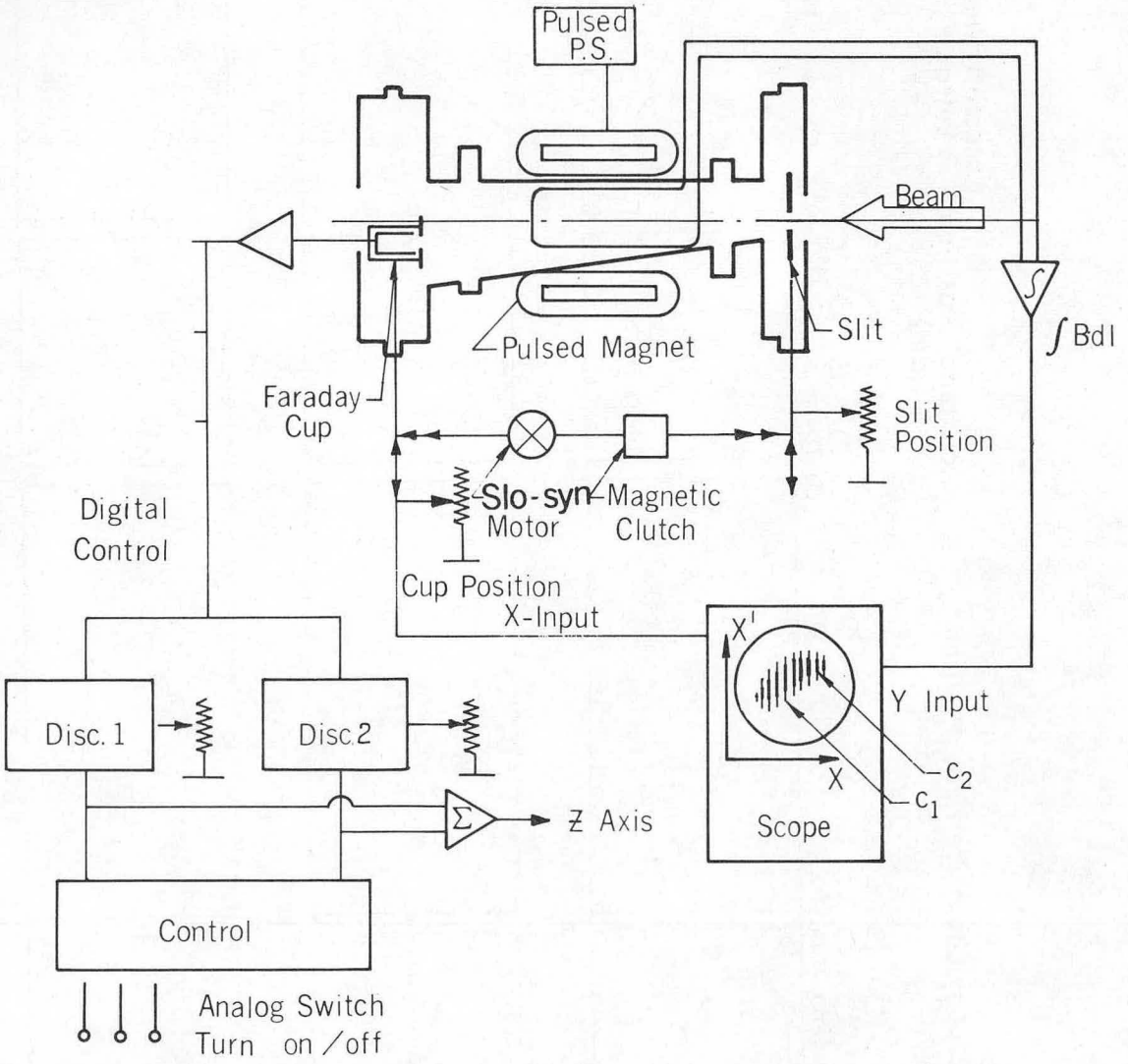

MUB-12713

Fig. 13

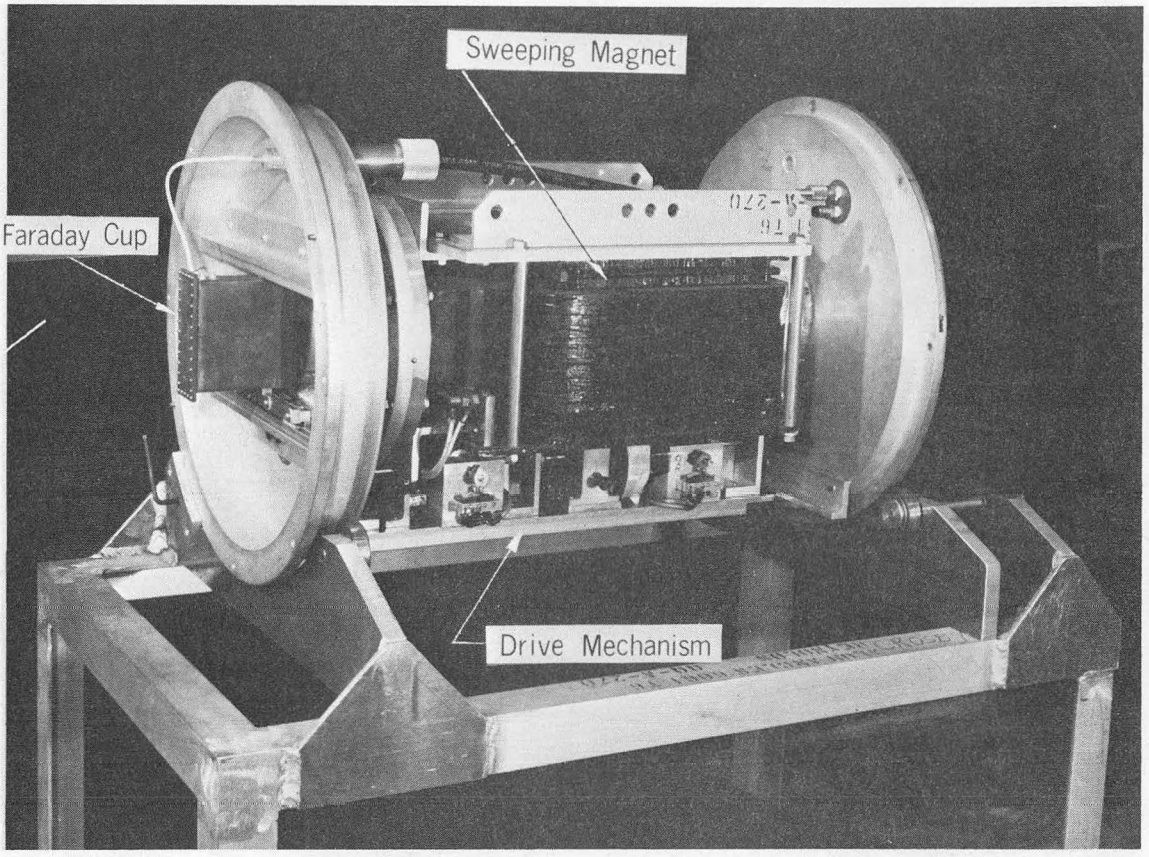

ZN-5914

Fig. 14

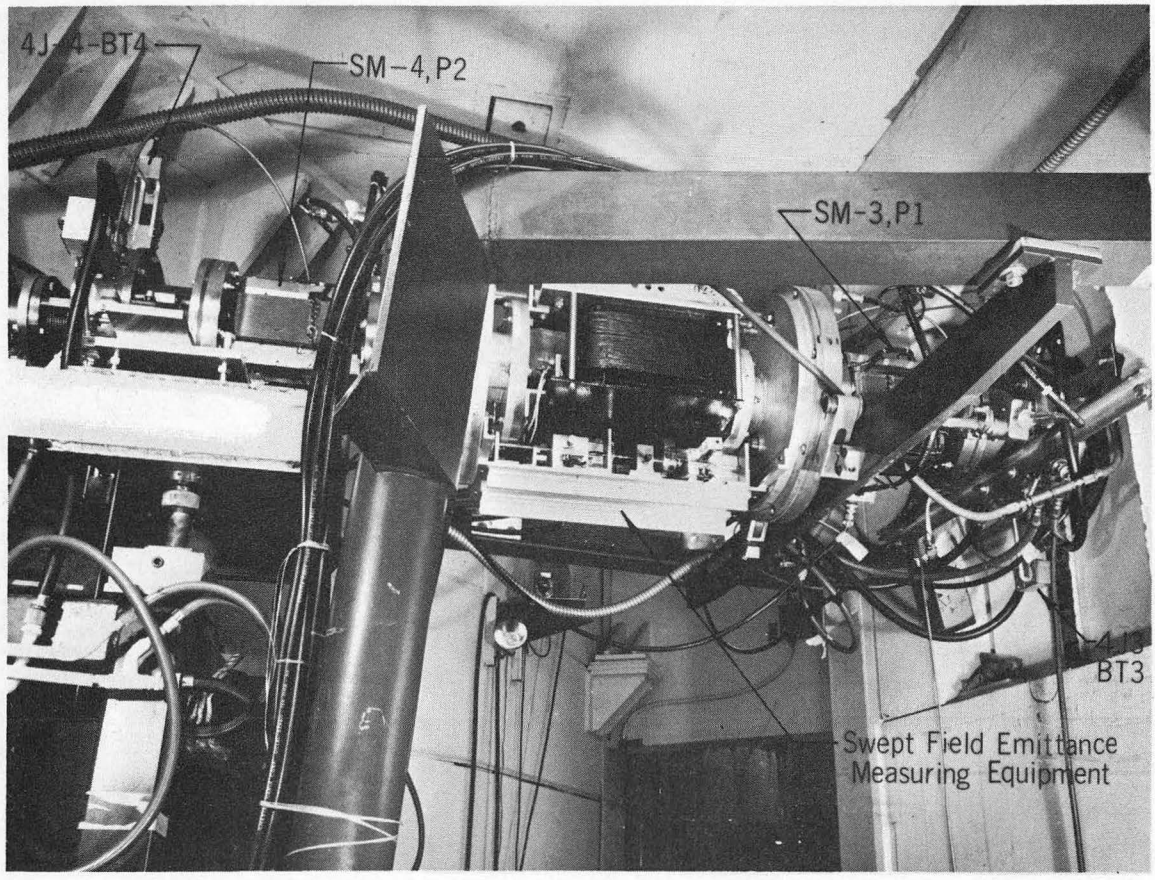

ZN-5918

Fig. 15

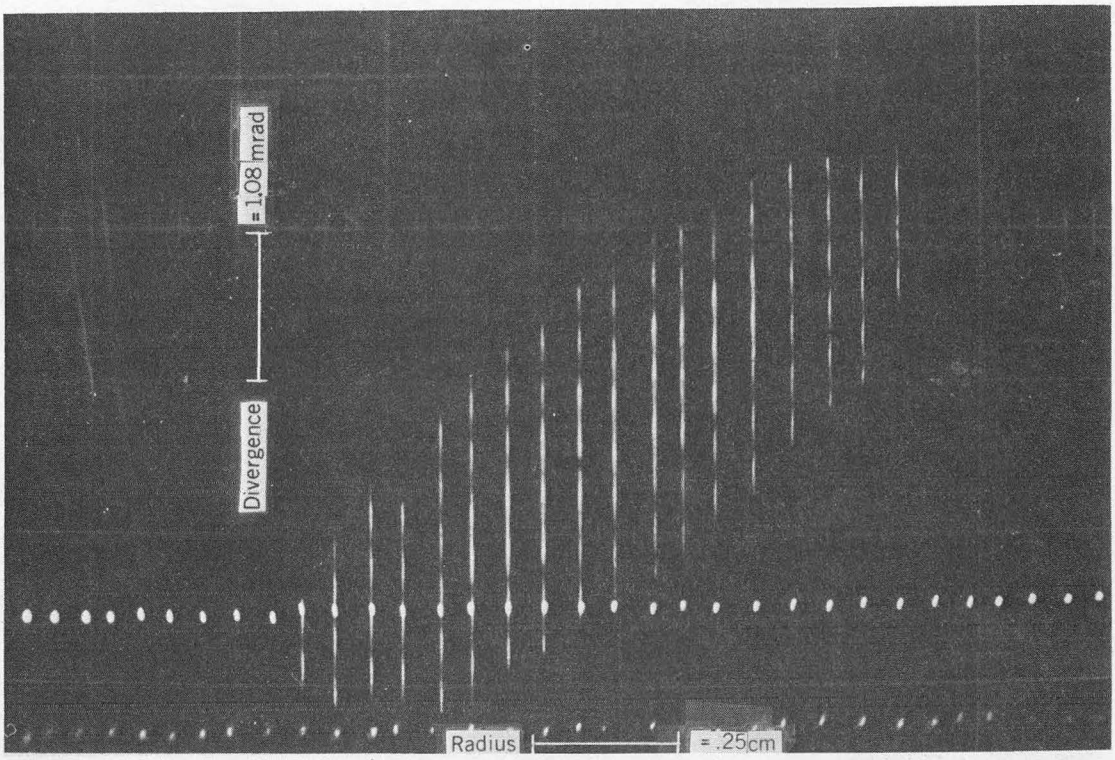

ZN-5942

Fig. 16

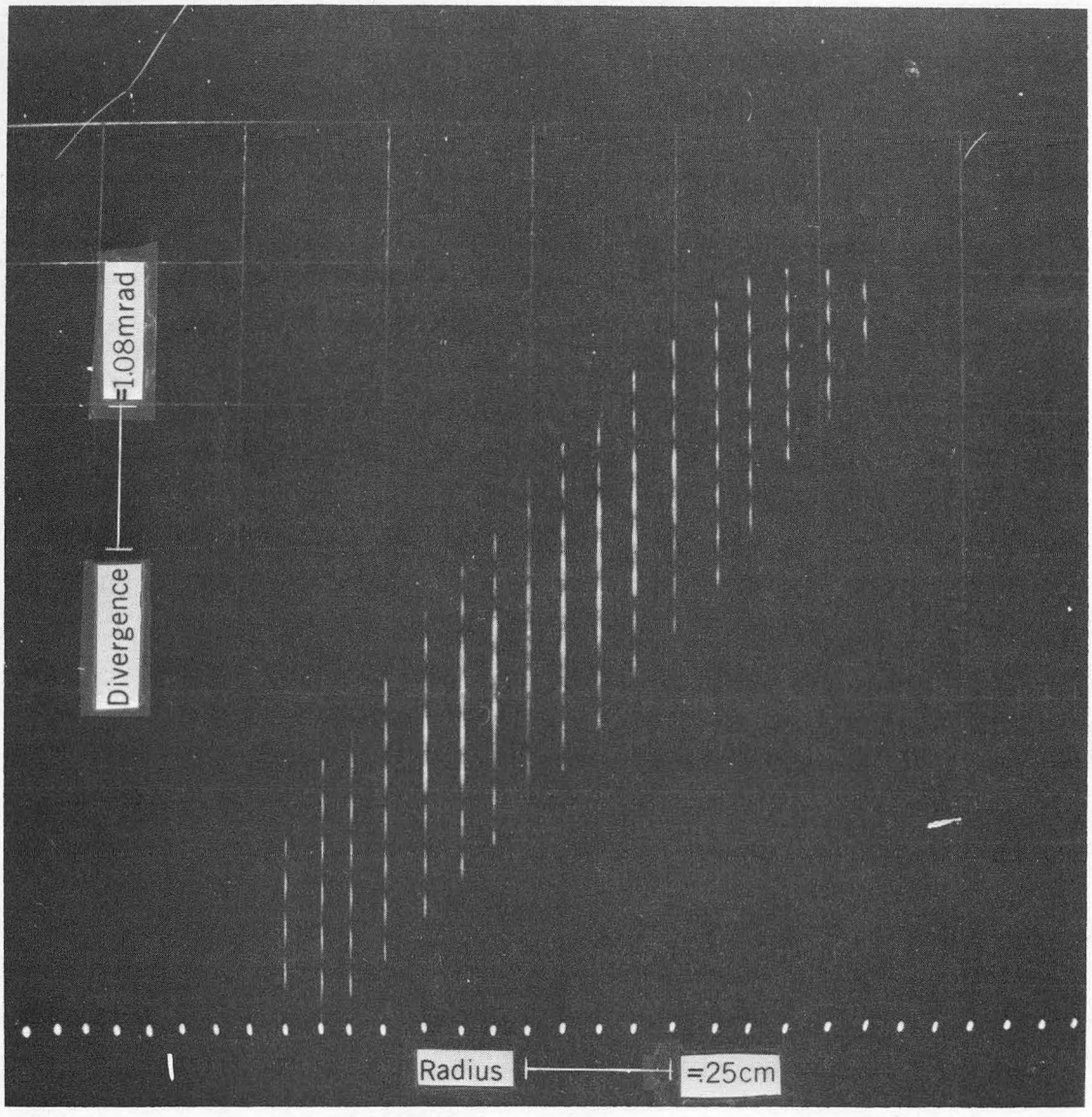

ZN-5943

Fig. 17

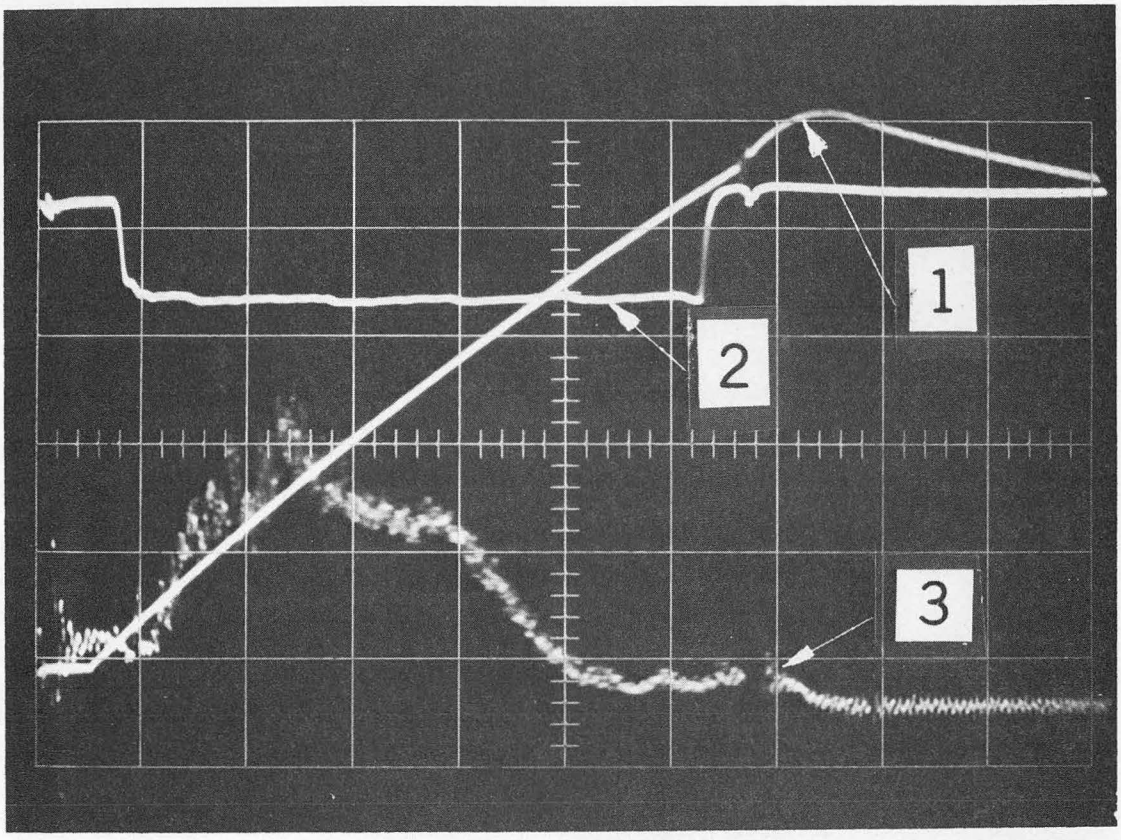

ZN-5919

Fig. 18

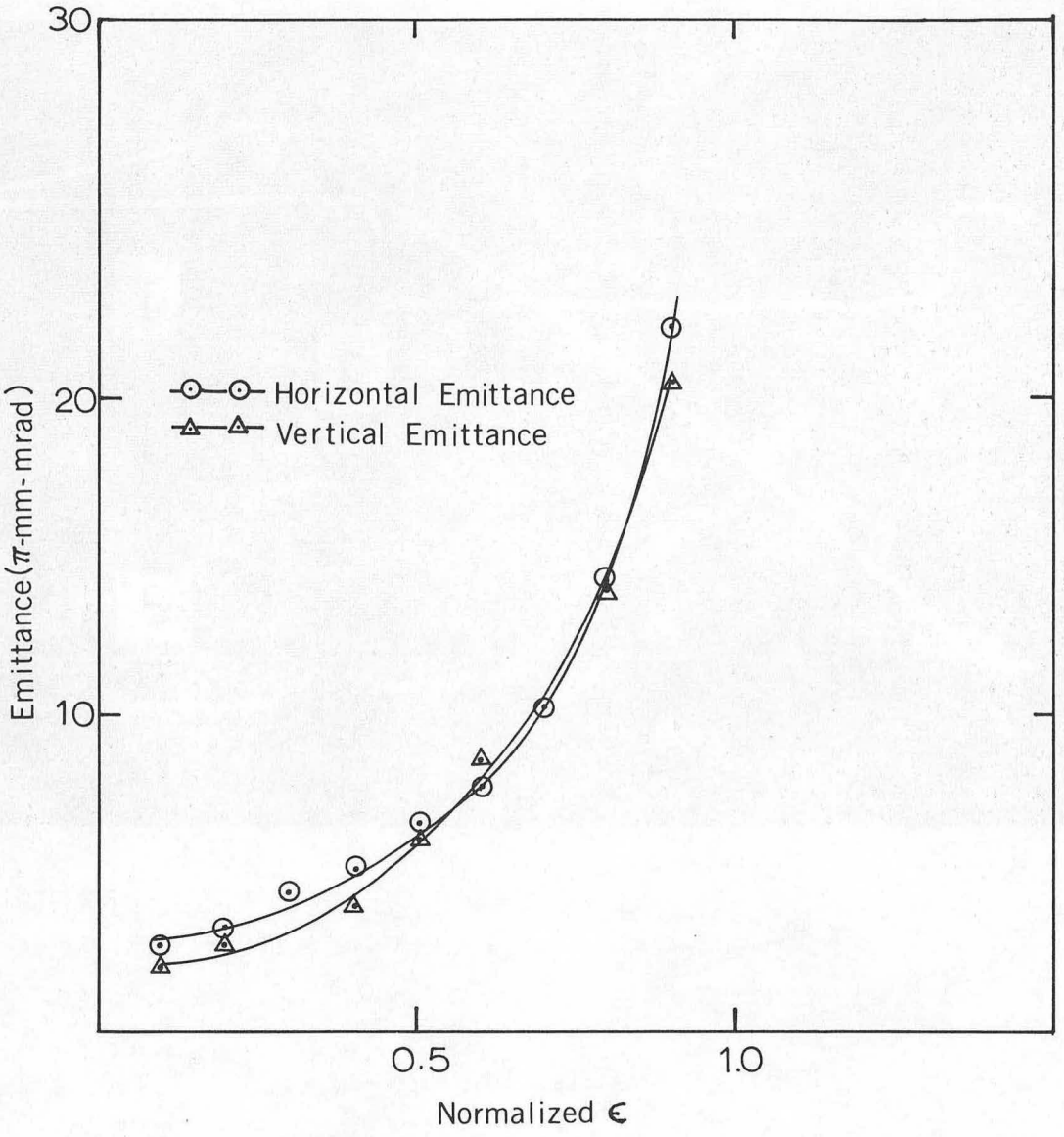

MUB-12894

Fig. 19

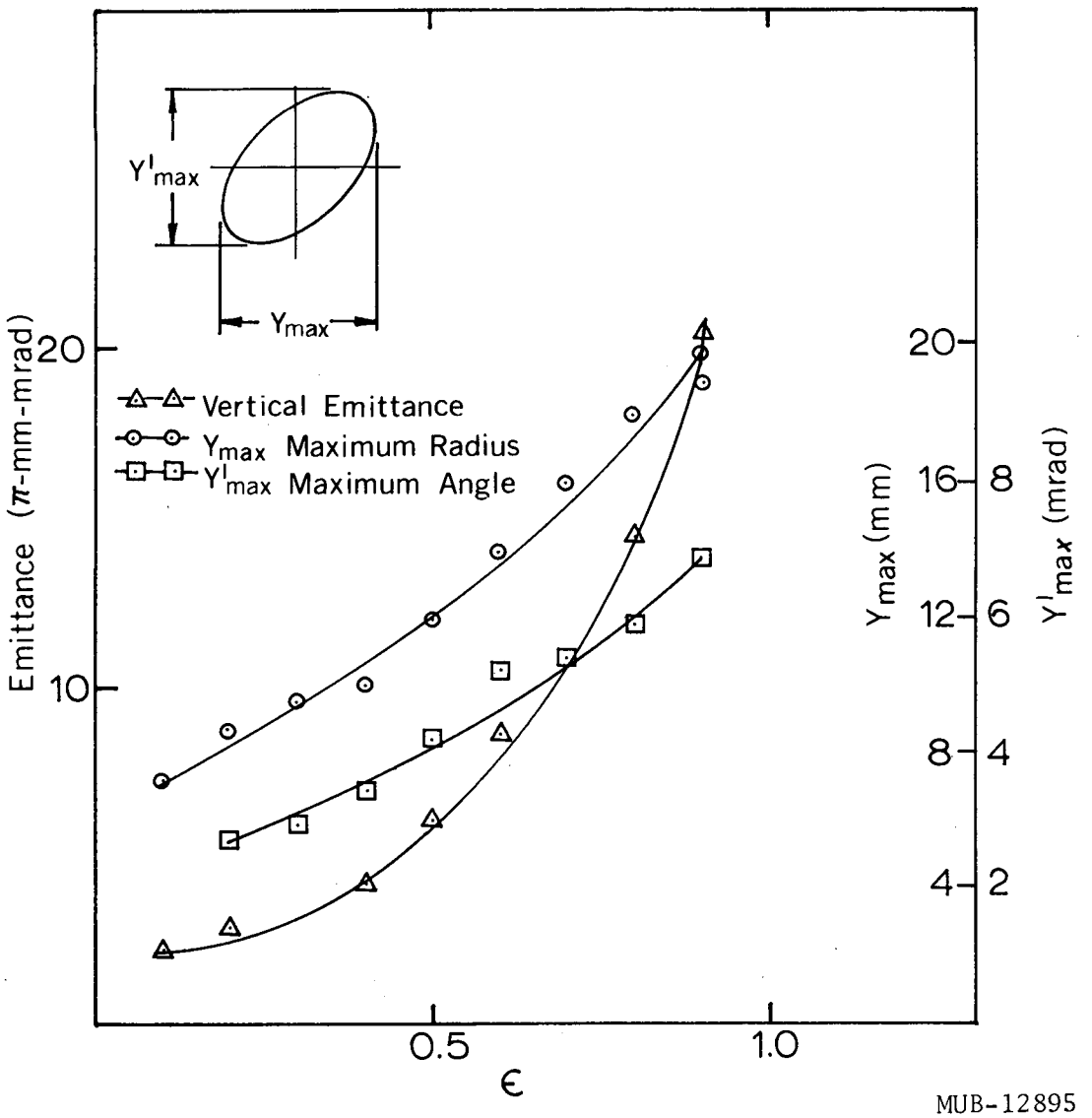
Y'max
Ymax
Vertical Emittance
Ymax Maximum Radius
Y'max Maximum Angle
Emittance (π-mm-mrad)
20
10
0.5
1.0
ϵ
20
16
12
8
4
Ymax (mm)
8
6
4
2
Y'max (mrad)
MUB-12895

Fig. 20

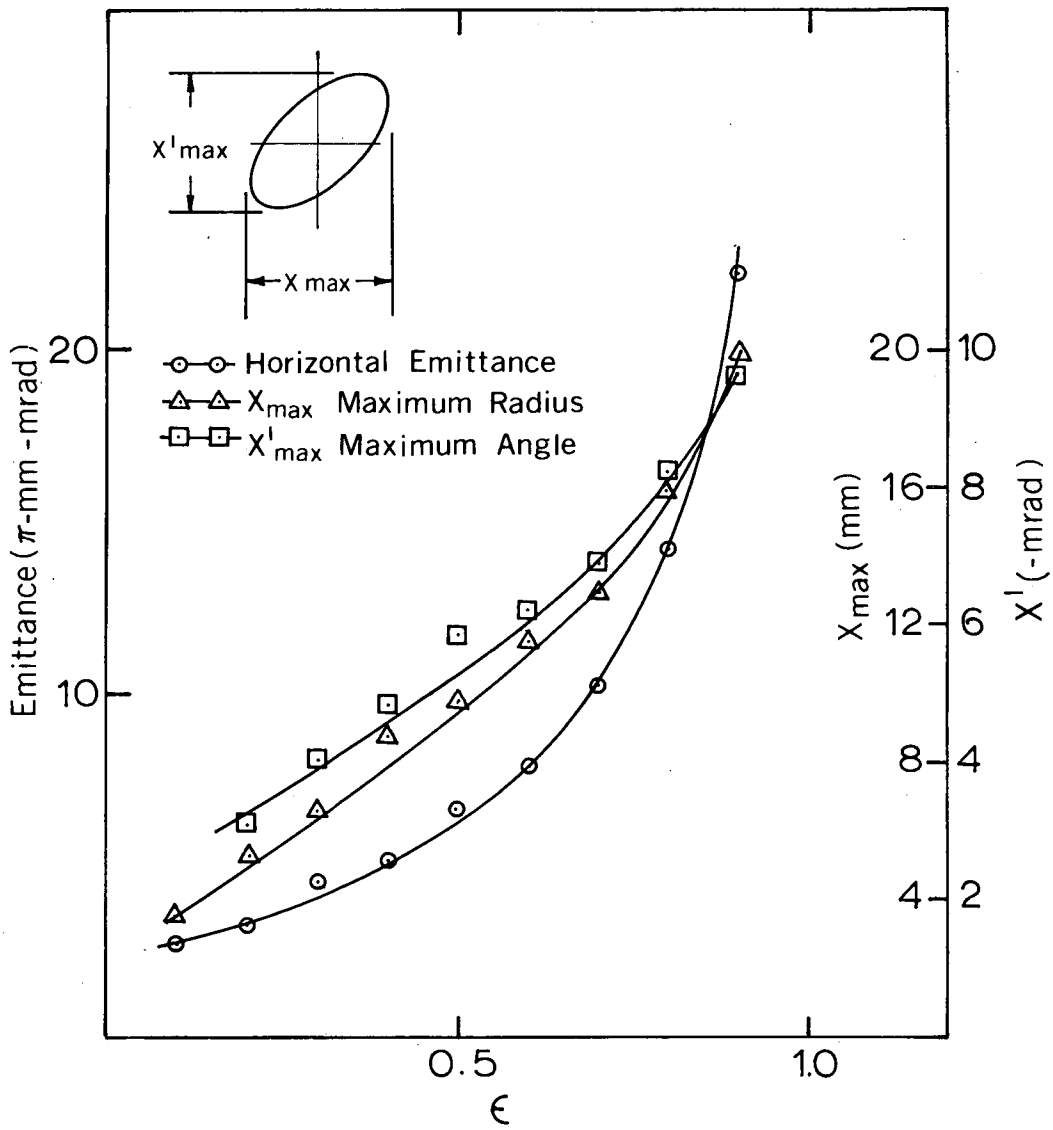
X'max
X max
Horizontal Emittance
Xmax Maximum Radius
X'max Maximum Angle
Emittance (π-mm-mrad)
20
10
0.5
1.0
ϵ
Xmax (mm)
X' (-mrad)
16
12
8
4
8
6
4
2
MUB-12715

Fig. 21

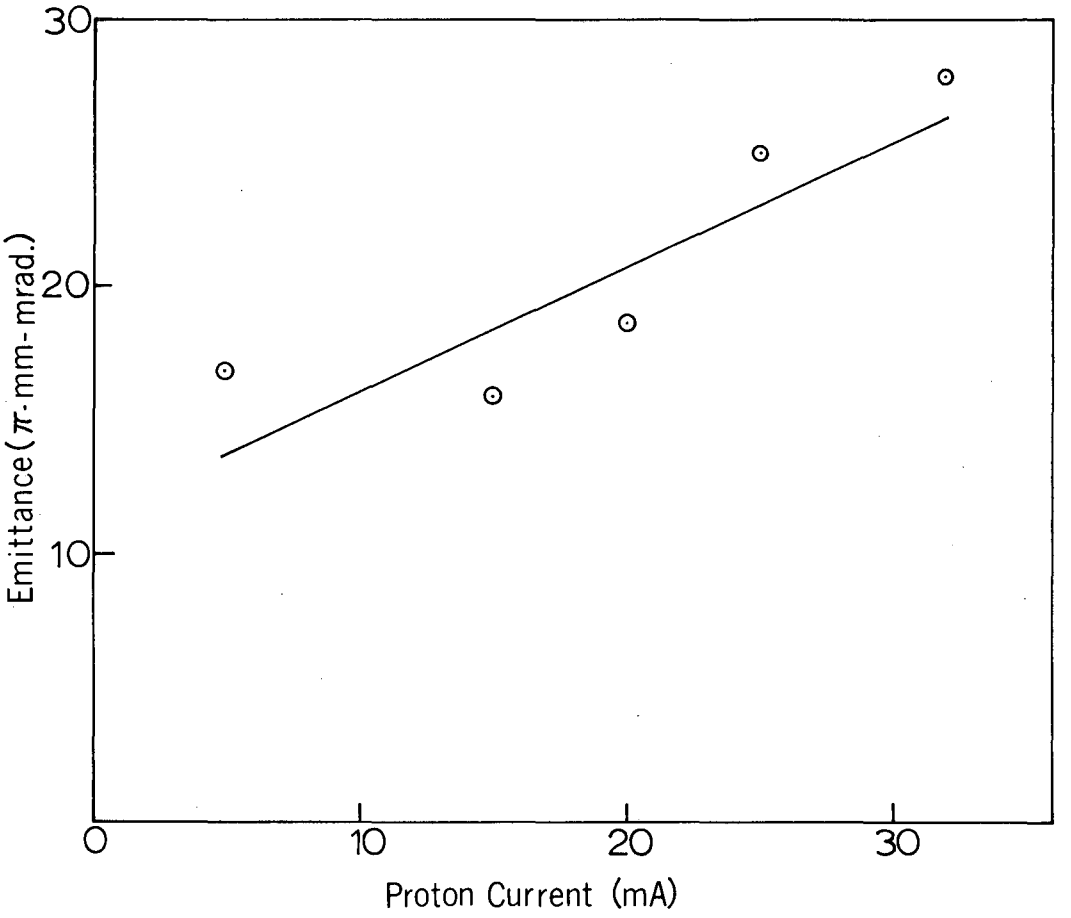

MUB-12896

Fig. 22

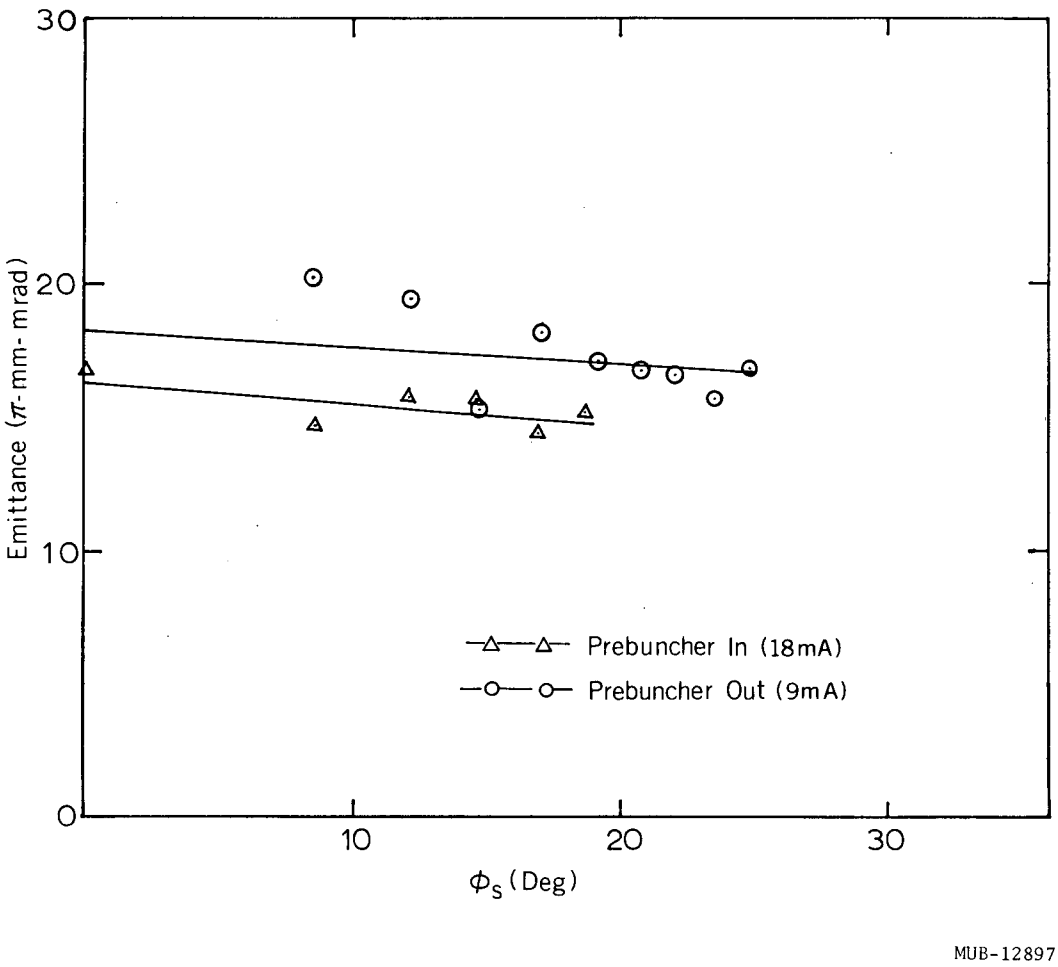
30
20
10
0
Emittance (π-mm-mrad)
10
20
30
ϕ_s (Deg)
Prebuncher In (18mA)
Prebuncher Out (9mA)
MUB-12897

Fig. 23

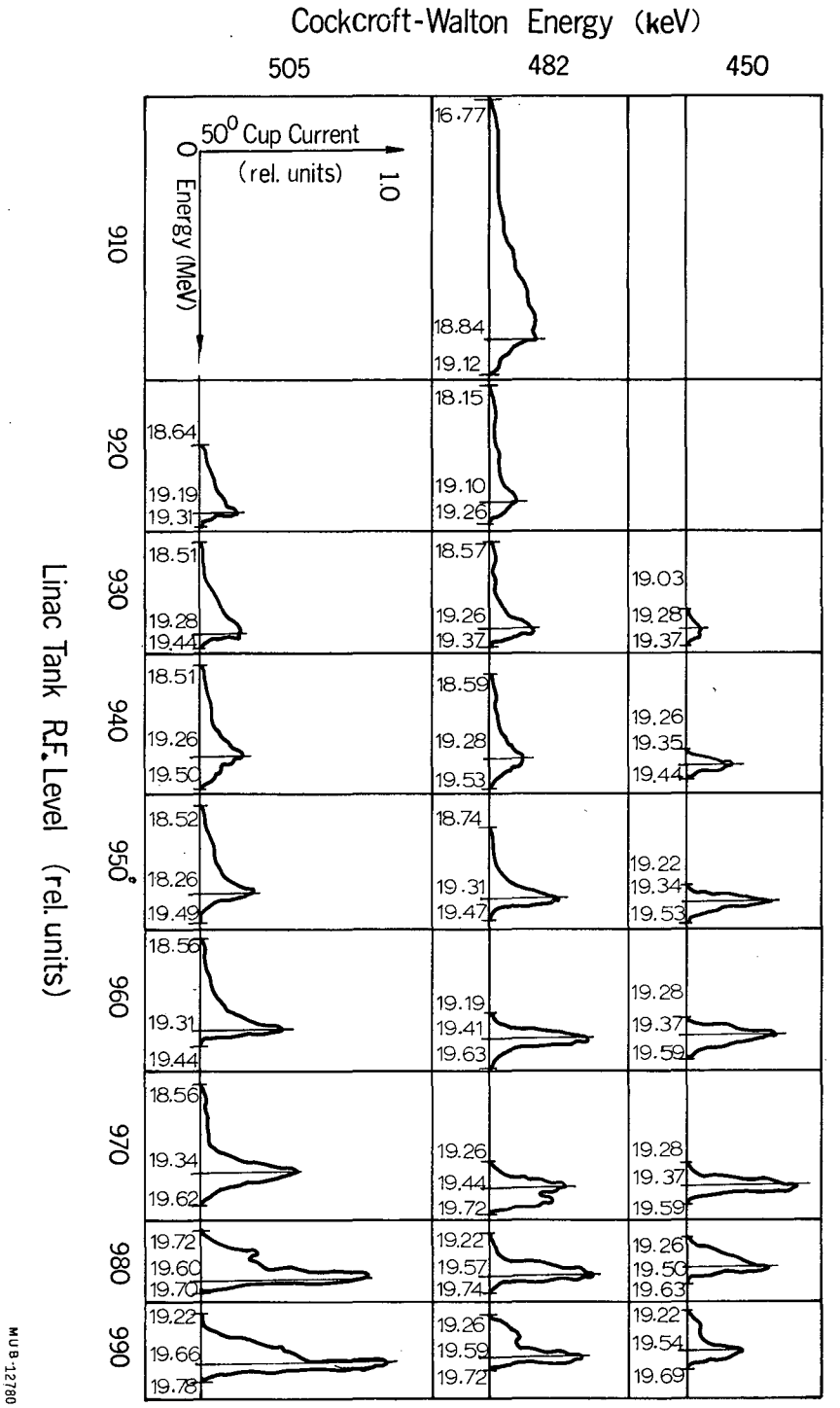

MU B-12780

Fig. 24

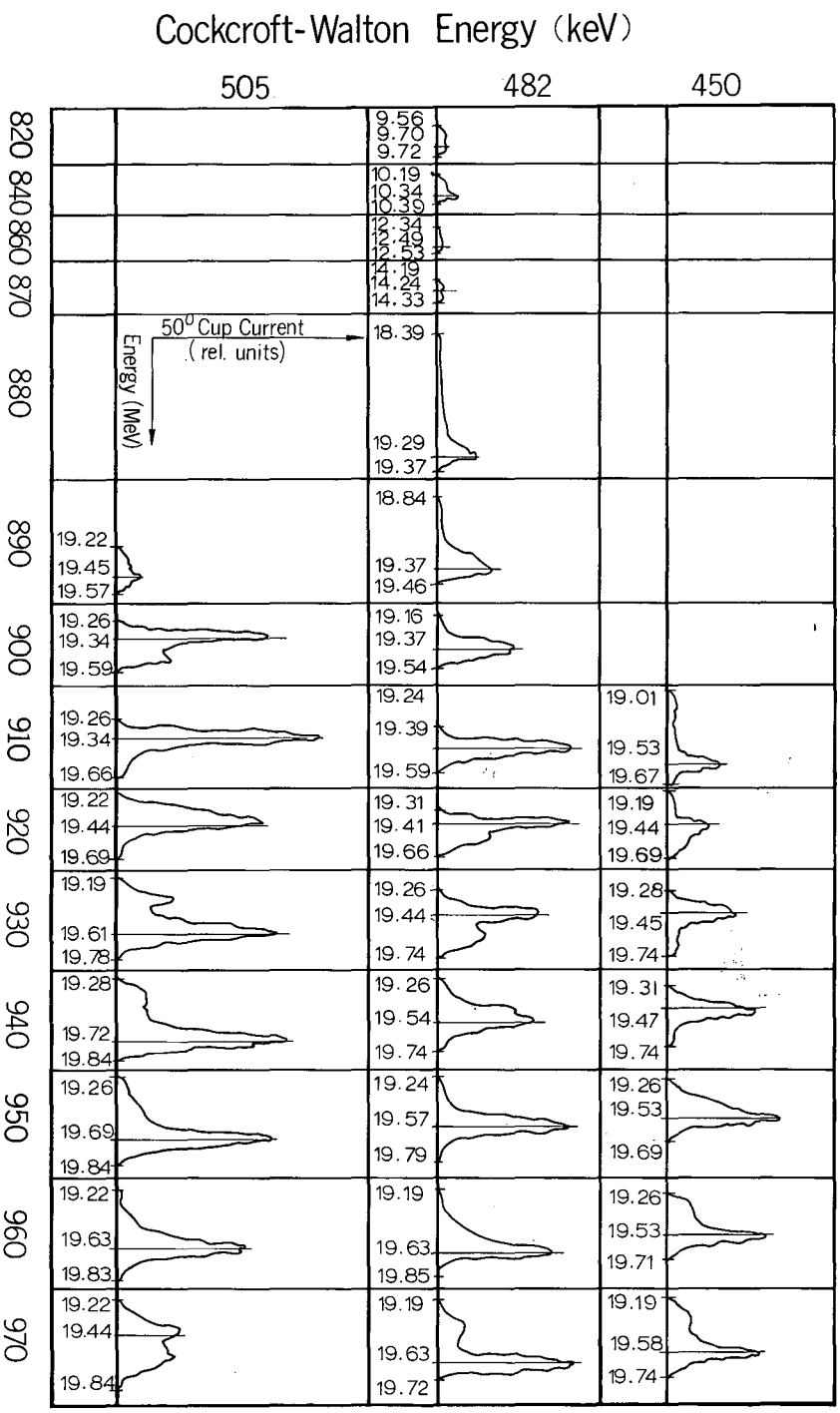
Cockcroft-Walton Energy (keV)
505
482
450
820 840 860 870 880 890 900 910 920 930 940 950 960 970
Linac Tank R.F. Level (rel. units)
Energy (MeV)
50° Cup Current
(rel. units)
9.56
9.70
9.72
10.19
10.34
10.39
14.19
14.24
14.33
18.39
19.29
19.37
18.84
19.22
19.45
19.57
19.37
19.46
19.26
19.34
19.59
19.16
19.37
19.54
19.24
19.39
19.59
19.01
19.53
19.67
19.26
19.34
19.66
19.22
19.44
19.69
19.31
19.41
19.66
19.19
19.44
19.69
19.19
19.61
19.78
19.26
19.44
19.74
19.28
19.45
19.74
19.28
19.72
19.84
19.26
19.54
19.74
19.31
19.47
19.74
19.26
19.69
19.84
19.24
19.57
19.79
19.26
19.53
19.69
19.22
19.63
19.83
19.19
19.63
19.85
19.26
19.53
19.71
19.22
19.44
19.84
19.19
19.63
19.72
19.19
19.58
19.74

Fig. 25

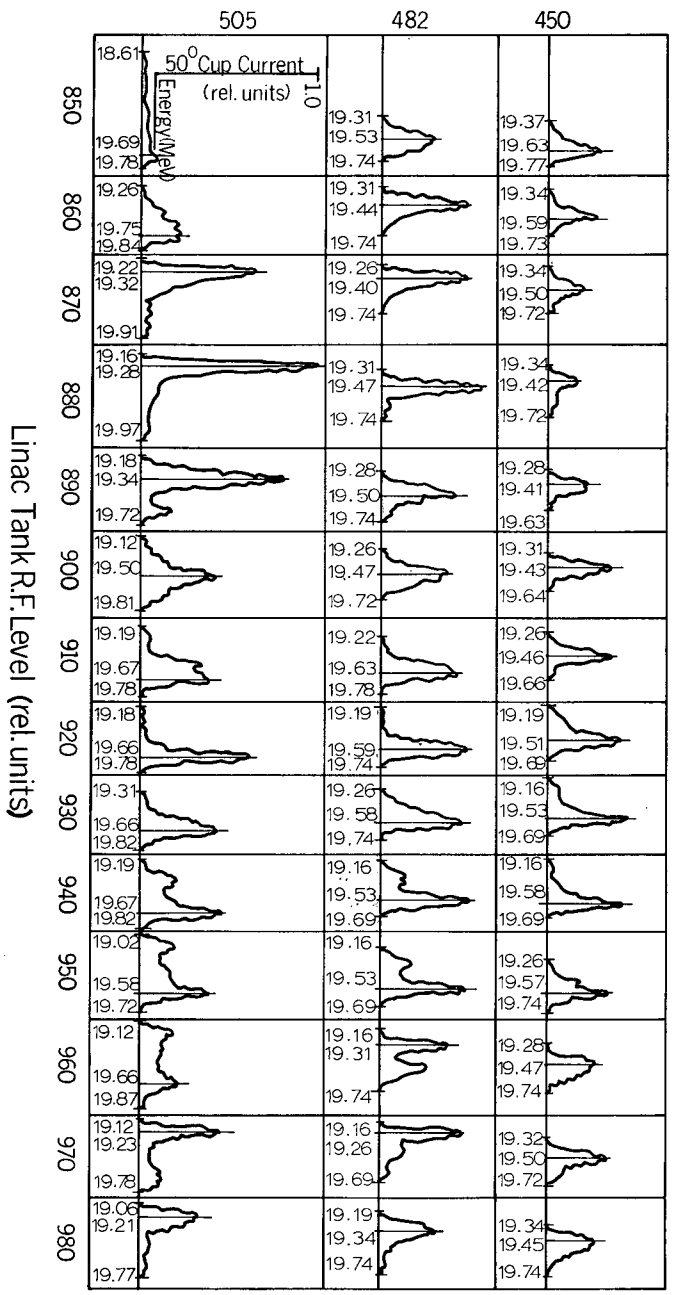
Cockcroft-Walton Energy (keV)
505
482
450
50° Cup Current
(rel. units)
1.0
Energy (MeV)
Linac Tank R.F. Level (rel. units)
850
860
870
880
890
900
910
920
930
940
950
960
970
980
18.61
19.69
19.78
19.26
19.75
19.84
19.22
19.32
19.91
19.16
19.28
19.97
19.18
19.34
19.72
19.12
19.50
19.81
19.19
19.67
19.78
19.18
19.66
19.78
19.31
19.66
19.82
19.19
19.67
19.82
19.02
19.58
19.72
19.12
19.66
19.87
19.12
19.23
19.78
19.06
19.21
19.77
19.31
19.53
19.74
19.31
19.44
19.74
19.26
19.40
19.74
19.31
19.47
19.74
19.28
19.50
19.74
19.26
19.47
19.72
19.22
19.63
19.78
19.19
19.59
19.74
19.26
19.58
19.74
19.16
19.53
19.69
19.16
19.53
19.69
19.16
19.31
19.74
19.16
19.26
19.69
19.19
19.34
19.74
19.37
19.63
19.77
19.34
19.59
19.73
19.34
19.50
19.72
19.34
19.42
19.72
19.28
19.41
19.63
19.31
19.43
19.64
19.26
19.46
19.66
19.19
19.51
19.69
19.16
19.53
19.69
19.16
19.58
19.69
19.26
19.57
19.74
19.28
19.47
19.74
19.32
19.50
19.72
19.34
19.45
19.74
MUB-12790

Fig. 26

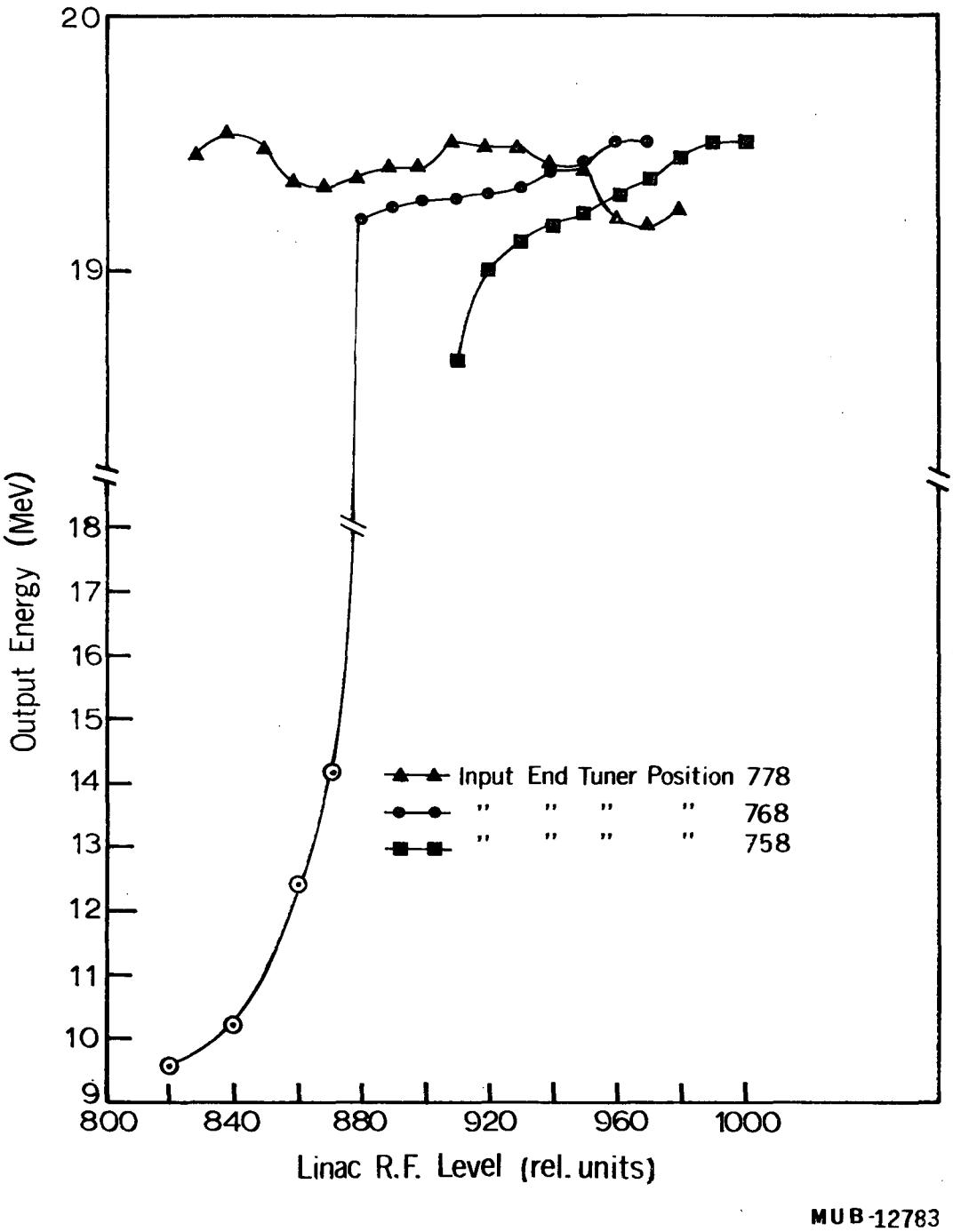
20
19
18
17
16
15
14
13
12
11
10
9
Output Energy (MeV)
800
840
880
920
960
1000
Linac R.F. Level (rel. units)
Input End Tuner Position 778
" " " " 768
" " " " 758
MUB-12783

Fig. 27

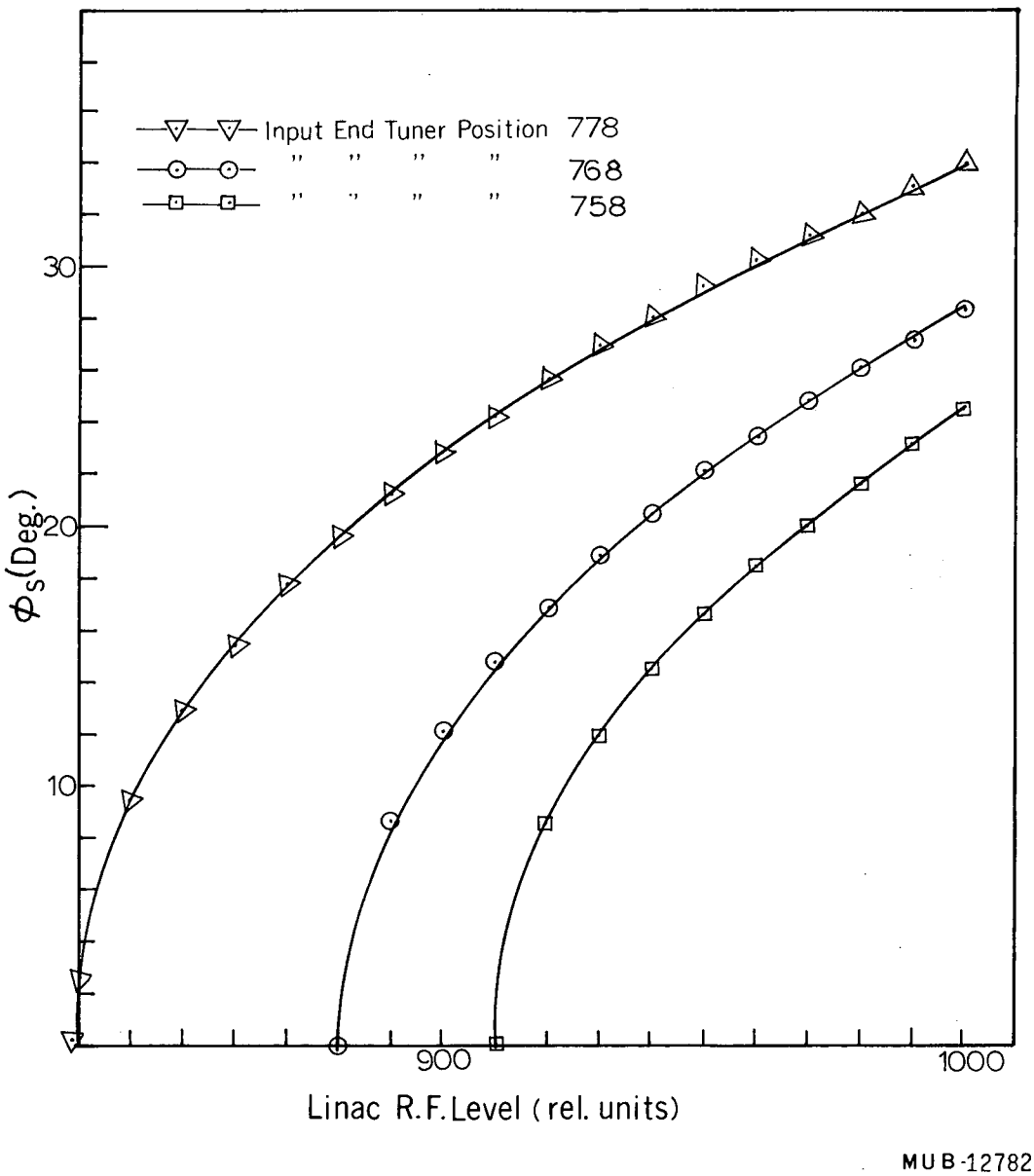
Input End Tuner Position 778
" " " " 768
" " " " 758
30
20
10
ϕ_s(Deg.)
900
1000
Linac R.F. Level (rel. units)
MUB-12782

Fig. 28

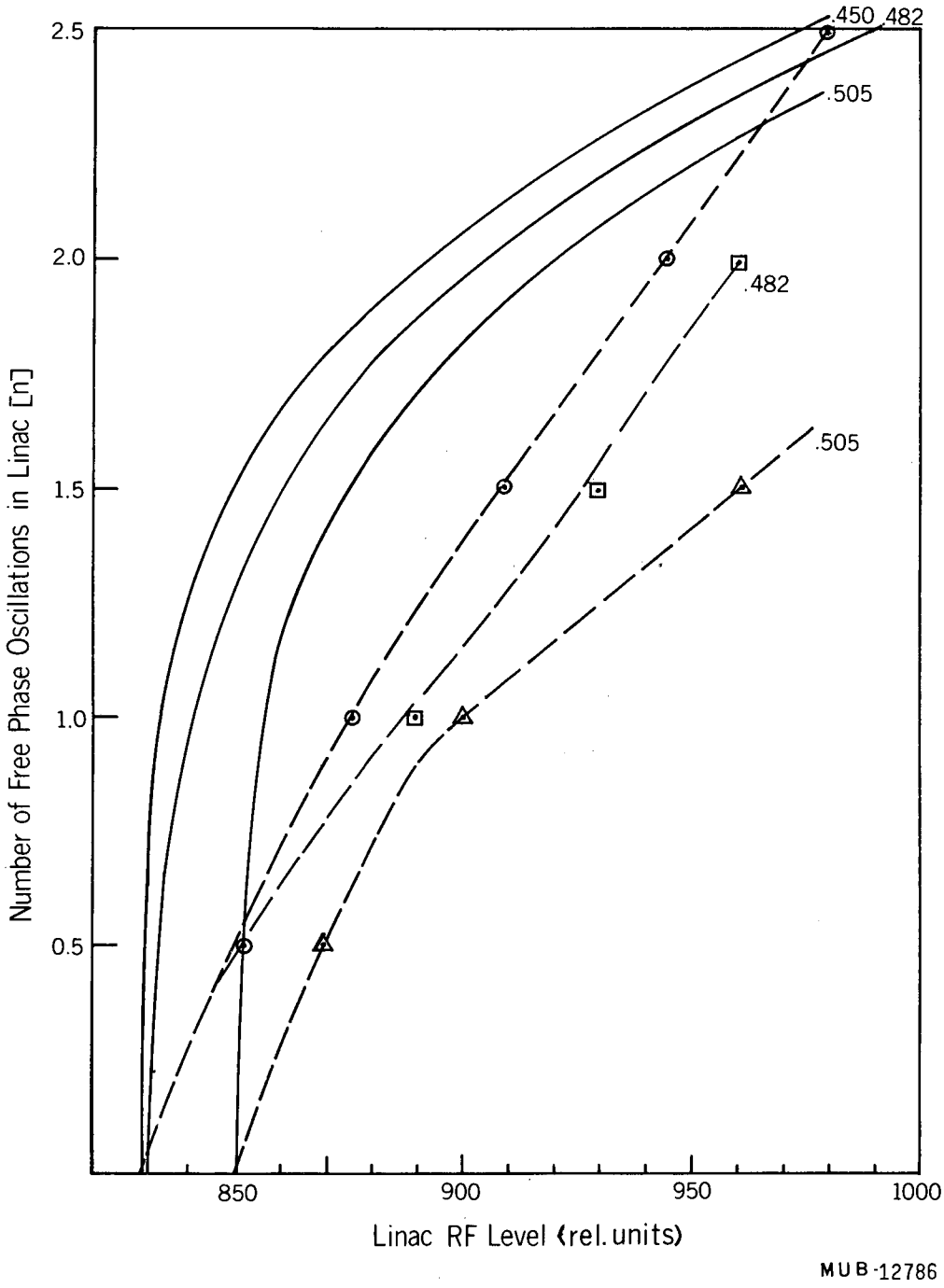
.450
.482
.505
.482
.505
2.5
2.0
1.5
1.0
0.5
Number of Free Phase Oscillations in Linac [n]
850
900
950
1000
Linac RF Level (rel. units)
MUB-12786

Fig. 29

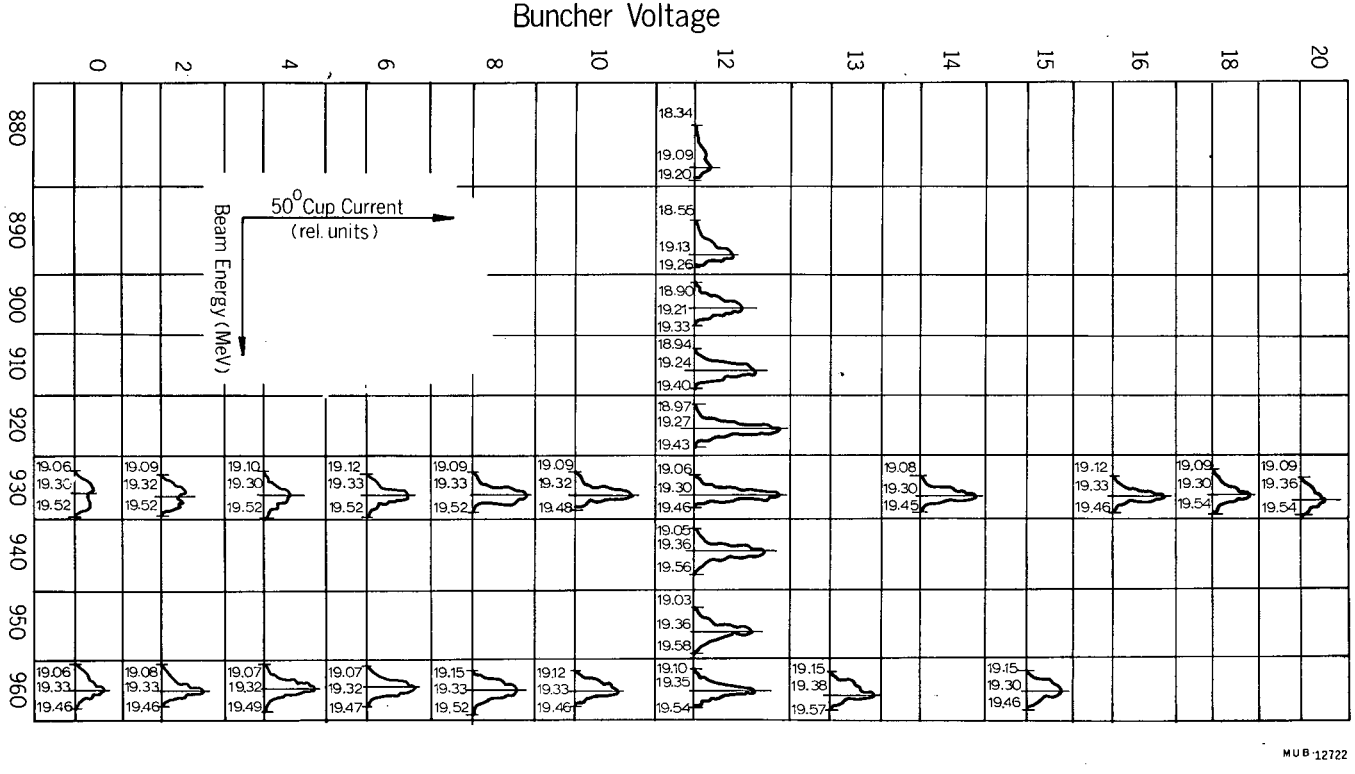

Linac Tank R.F. Level

Fig. 30

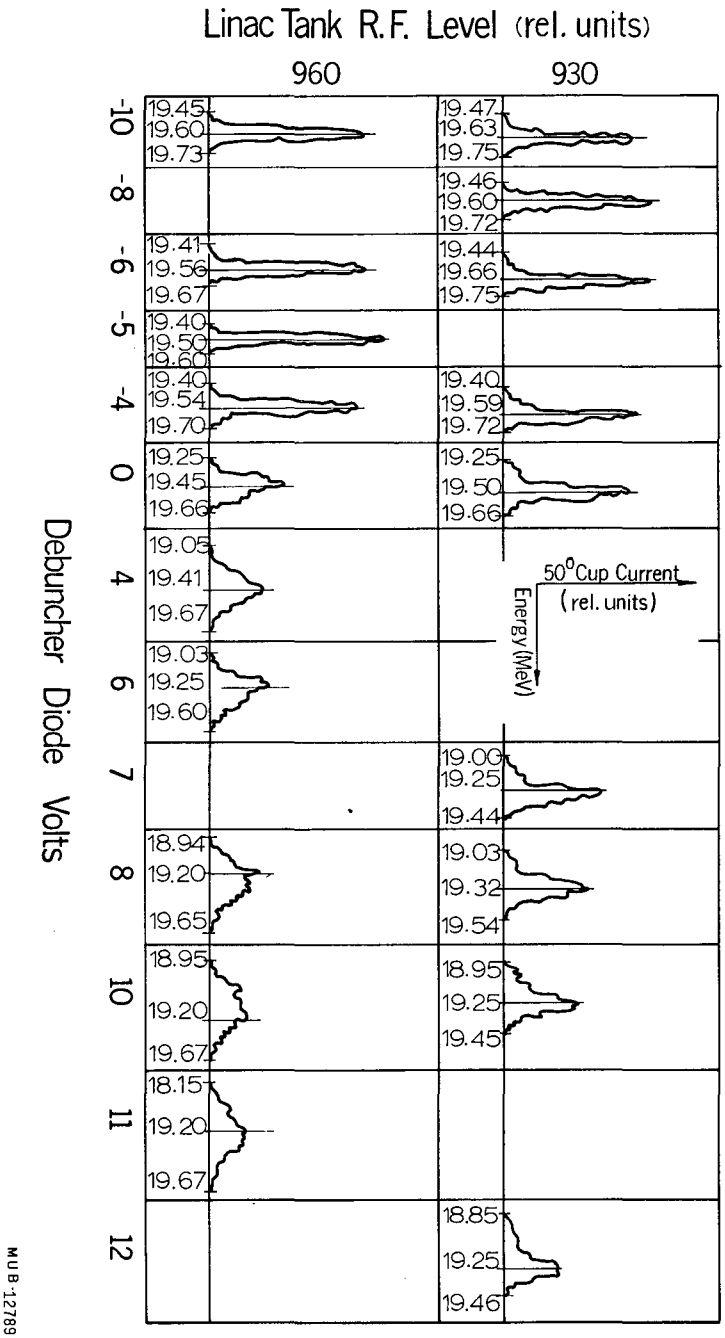
Linac Tank R.F. Level (rel. units)
960
930
Debuncher Diode Volts
-10
-8
-6
-5
-4
0
4
6
7
8
10
11
12
19.45
19.60
19.73
19.47
19.63
19.75
19.46
19.60
19.72
19.41
19.56
19.67
19.44
19.66
19.75
19.40
19.50
19.60
19.40
19.54
19.70
19.40
19.59
19.72
19.25
19.45
19.66
19.25
19.50
19.66
19.05
19.41
19.67
50° Cup Current
(rel. units)
Energy (MeV)
19.03
19.25
19.60
19.00
19.25
19.44
18.94
19.20
19.65
19.03
19.32
19.54
18.95
19.20
19.67
18.95
19.25
19.45
18.15
19.20
19.67
18.85
19.25
19.46
MUB-12789

Fig. 31